Optimal nonequilibrium driving of a rotary mechanochemical motor

by

Aliakbar Mehdizadeh

B.Sc., Sharif University of Technology, 2014

Thesis Submitted in Partial Fulfillment of the
Requirements for the Degree of
Master of Science

in the
Department of Physics
Faculty of Science

SIMON FRASER UNIVERSITY
Fall 2016

Approval

Name:	**Aliakbar Mehdizadeh**
Degree:	**Master of Science (Physics)**
Title:	***Optimal nonequilibrium driving of a rotary mechanochemical motor***
Examining Committee:	**Chair:** Dr. Stephanie Simmons Assistant Professor

Dr. David Sivak
Senior Supervisor
Assistant Professor _____

Dr. Eldon Emberly
Supervisor
Associate Professor _____

Dr. Nancy Forde
Internal Examiner
Associate Professor _____

Date Defended: 24 November 2016

Abstract

Prompted by current experiments on mechanically driven F_1 ATP synthase, we investigate optimal (minimum-dissipation) driving protocols of rotary mechanochemical motors. We propose a simple model system coupling chemical reactions to mechanical motion under periodic boundary conditions, driven by a periodic time-dependent force. Under linear response approximations near equilibrium and near nonequilibrium steady states, optimal driving protocols are determined by a generalized friction coefficient. Such a model has a periodic generalized friction coefficient that peaks near system energy barriers, implying optimal protocols that proceed rapidly when the system is overwhelmingly in a single macrostate, but slow significantly near energy barriers, harnessing thermal fluctuations to kick the system over the energy barriers for free.

Keywords: nonequilibrium thermodynamics; stochastic physics; optimal driving protocol

Dedication

This thesis is dedicated to my parents.

Acknowledgements

First of all, I would like to express my sincere gratitude to my senior supervisor Dr. Sivak for the continuous support through both my study and research, and for his enthusiasm that kept me motivated over the past semesters. I am also indebted to my supervisory committee member, Dr. Emberly, and teachers, all of whom taught me with patience. I would also like to thank all of the members of the Sivak research group, especially S. Large, A. Kasper, A. Brown, and J. Lucero for all the constructive enlightening discussions, suggestions, and comments on this project. Special thanks to the staff of the Physics Department, they helped me restlessly from the very first day.

Last but not the least, I would like to thank my parents and my brother for being so supportive over these years.

Table of Contents

List of Figures

Chapter 1

Introduction

Living organisms obtain energy, move around, produce products, waste energy, and perceive the world around them to perform a wide variety of biological tasks [1]. These biological tasks are believed to be accomplished by cooperation and contribution of various biological actors such as different molecular motors, in mechanisms considerably different from human-made large-scale motors. One central distinction of biological processes and everyday macroscopic processes is the key role of temperature, more specifically thermal fluctuation. Familiar robust macroscopic machines—such as car engines—can perform in a wide range of temperatures, but living processes are much more sensitive to the actual temperature of the environment, and they often stop functioning properly outside small temperature variations. Considering the small physical dimensions of the biological motors, the energy scale on which many biological systems operate is close to the scale of thermal fluctuations, i.e. $k_{\mathrm{B}}T$. Therefore, thermal fluctuations are tremendously important and influential [2, 3] in the operation of molecular-scale biological systems. Moreover, many biological processes are found to be impressively efficient and rapid, often occurring on millisecond- or shorter timescales, which suggests efficient operation in the nonequilibrium thermodynamic regime [2, 4].

During recent decades, developments in experimental methods, theoretical frameworks, and mathematical modeling have provided both large data sets and significant complexity in our understanding of biological systems [1, 5]. This progress has made it more convenient and reasonable to describe biosystems quantitatively, where only qualitative explanations were formerly conceivable. This particular perspective has become more and more attainable by major progress achieved in nanometer-scale technologies such as construction of high-precision measurement instruments [6]. These subtle instruments provide essential infrastructures for profound interdisciplinary studies between biology and physics as well as sufficiently precise experimental equipment to quantitatively examine proposed theoretical frameworks in the field of nonequilibrium thermodynamics.

Molecular motors, in general, operate in strongly fluctuating environments, yet amazingly produce highly reliable results, operating in a way that differs drastically from more familiar human-sized machines. Death of a biological system can be equated with thermal equilibrium, where the system (such as a molecular motor) does not evince any preference (on average) to move forward or backward. Life thus seems to require directed operation involving nonequilibrium dynamics. But how can biological organisms self-organize and maintain their essential directed operation far away from equilibrium?

Dissipative physical systems (including biological systems) are open: they need a continual input of energy, matter (or both) from the environment, in order to maintain their capacity of doing useful work. In other words, much research points to this continual flux of energy within the physical boundaries of a dissipative system leading to the ability to self-organize, while operating in the nonequilibrium thermodynamic regime [7]. While equilibrium thermodynamics was primarily developed (and reached relative maturity) during the 19th century, nonequilibrium thermodynamics is a newly emerging field of physics. In this regard, life (and more specifically molecular motors) seems to be a set of interesting naturally available and evolutionarily tuned objects that operate mostly far away from equilibrium, providing a number of promising biological systems for collaborative investigation between both physicists and biologists, theorists and experimentalists.

Much current investigation seeks to understand the remarkable features of molecular motors, especially features crucial to machines of such size [2]. For instance, researchers are investigating the unique cyclical operations of small biological machines that are responsible for converting chemical energy sources (most notably adenosine triphosphate [ATP]) into useful mechanical work [8]. The experimentally measured mechanical efficiency of this mechanochemical molecular motor under high viscous loading is nearly 100%, significantly higher than other biological motor proteins that are driven by hydrolysis of ATP molecules [9]. This highly efficient operation stimulates great interest in characterizing the limits of efficient stochastic operation of stochastic mechanochemical motors, as well as understanding the properties of optimal driving protocols [10, 11, 12, 13, 14]. In particular, it would be informative to answer the following questions regarding the efficient operation of stochastic motors: What is the highest possible energy conversion efficiency rate for biological stochastic motors that are driven in finite time intervals? What sort of interactions with the external energy resources lead physical systems to achieve the greatest possible efficiency? How much energy the optimal, minimum-dissipation, driving protocols save compared to more naive, driving protocols?

1.1 Molecular motors

Motor proteins play a key role in many essential cellular processes. For example, three families of molecular motors (myosin, kinesin, and dynein) power a wide variety of intra-

cellular movements [15]. In response to new experimental and theoretical developments, fundamental principles of small-scale stochastic motor design and operation have been proposed [16, 17, 18, 19, 20, 21, 22]. These design principles introduce nonequilibrium driving protocols in order to effectively harness thermal fluctuations and to ultimately optimize the stochastic system's dissipation and hence energy expenditure. Molecular machines generally use chemical energy to do useful work either in rotary or in linear motions that are often essential for controlling and managing a broad set of other biological processes.

Advances in their understanding have led to significant progress in the construction of small stochastic objects and processes, such as sensors, transporters, and actuators [23, 24, 25].

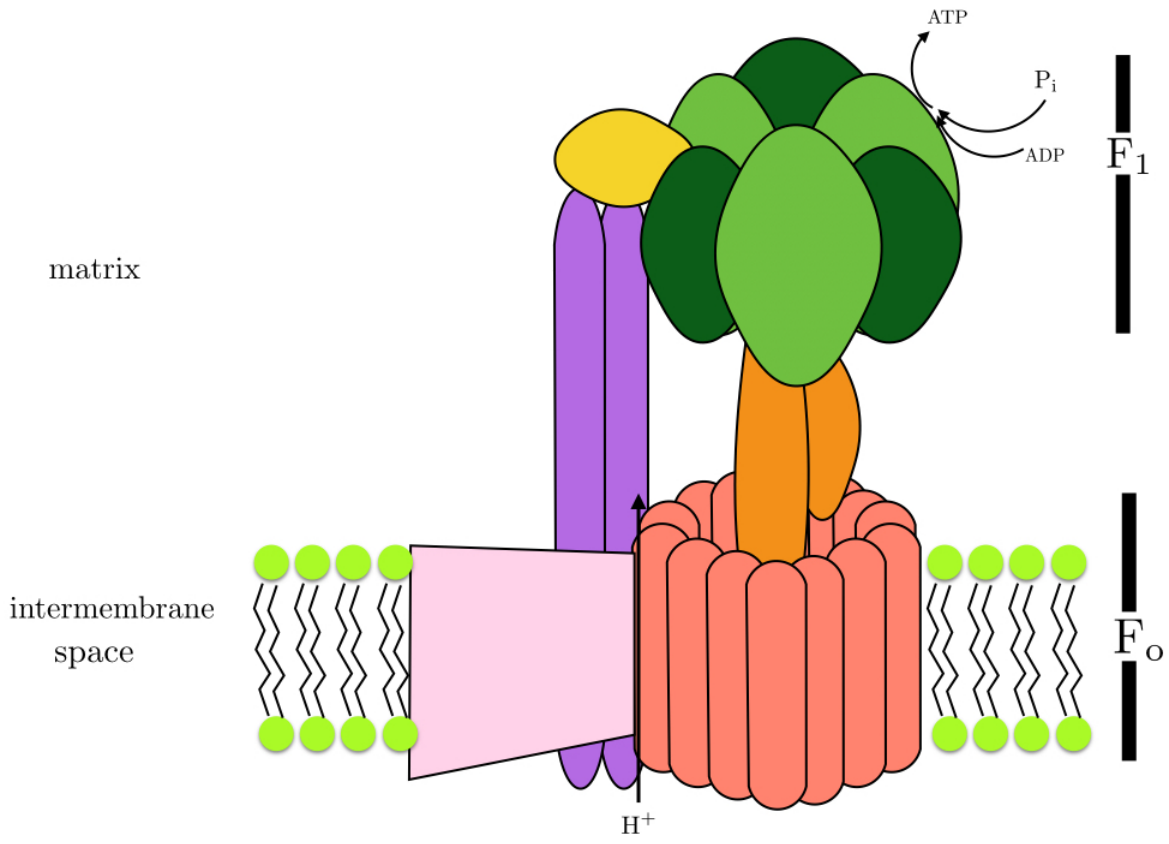

Figure 1.1: Schematic representation of the F_oF_1 ATP synthase, a rotary molecular machine coupling the chemical reaction of ATP-ADP conversion with mechanical rotation in order to produce high energy ATP molecules from low energy ADP molecules *in vivo*. ATP synthase is believed to be powered by proton flow across the intermembrane region such that proton flow rotates the central crankshaft connecting F_1 and F_o regions, that ultimately stimulates ATP production in F_1's three catalytic sites which are represented by dark green sub-unite. See Fig. 1.2 for more details.

Molecular motors typically operate stochastically far from equilibrium regime, immersed in an thermal bath, where the state of the molecular environment and thermal fluctuations are expected to be critically important and effective. Therefore, an appropriate theoretical framework describing the physical principles of molecular machine performance should recognize their dynamic conformational changes, capture their coupling of mechanical motion and chemical activity, and successfully explain the striking features of motor proteins such as their high efficiency despite fast operation and large fluctuations.

1.2 F_oF_1 ATP synthase

In a wide variety of living organisms including bacteria, plants, and animals [26], a rotary membrane-bound motor protein is responsible for the synthesis of ATP molecules, the universal energy currency in living organisms. Our main focus in this research is on the mitochondrial version of this enzyme, composed of two regions, one directly catalyzing ATP synthesis (F_1) and one transporting protons down their gradient (F_o). These two regions are connected through a central mechanical crankshaft, capable of rotation in both clockwise and counterclockwise directions. In general, it is believed that ATP synthesis is driven by proton flow through the F_o region, from the intermembrane region into the mitochondrial matrix, and likewise it is believed that protons can also be pushed out, against the favorable concentration gradient, by ATP hydrolysis [27].

The F_1 region is a rotary molecular machine that has a structural three-fold symmetry. It contains three identical β subunits that catalyze the chemical synthesis and hydrolysis of ATP/ADP molecules. It has been proposed that these catalytic sites adopt different conformations corresponding to different angular orientations of the central crankshaft [26]. It is proposed that the different catalytic sites proceed through the same sequence of conformations, but at any given moment each one will be in a different phase (step) of the chemical reaction.

The chemical reaction has three separate steps. First, ADP molecules and P_i (phosphate) molecules bind, then ATP is synthesized, and finally ATP is released into the mitochondrial matrix. It is believed that the relative orientation of the central crankshaft stimulates a time-dependent conformational change within the catalytic sites, so that crankshaft rotation drives step-by-step production of ATP from ADP [26].

Given this proposed framework for F_1 ATP synthase structure and function, we would like to answer the following questions in the context of a simple thermodynamic model system, representing the basic features of this stochastic rotary mechanochemical molecular motor: What is the optimized schedule of mechanically perturbing such a molecular motor around a cycle of its operation that minimizes the demands for energy input from external energy resources? And how quantitatively and qualitatively do these optimal driv-

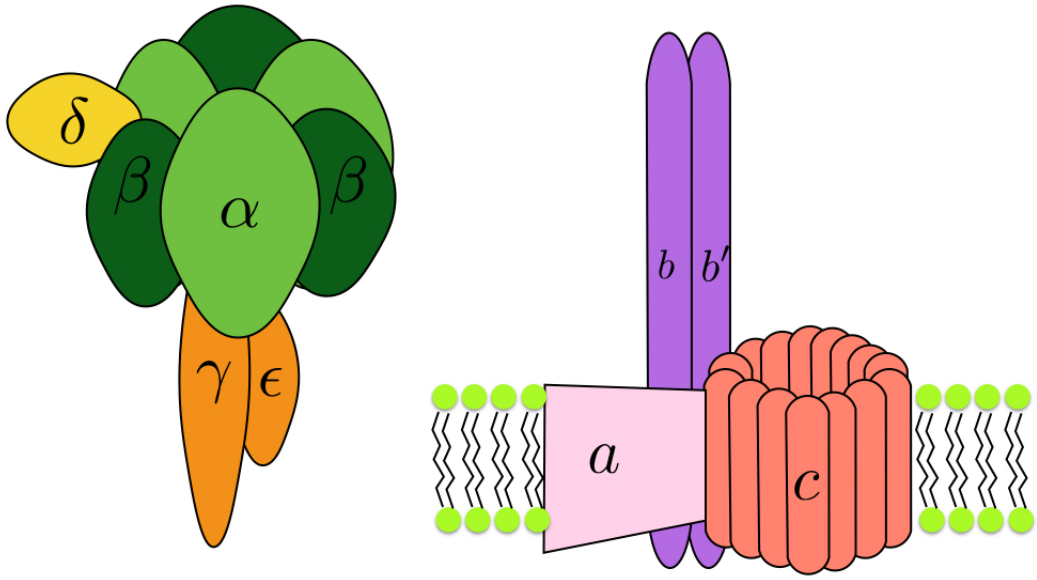

Figure 1.2: Schematic representation of the two main parts of F_oF_1 ATP synthase. Left: the F_1 component. Right: the F_o component. These two components are coupled by the central crankshaft.

ing protocols differ from naive protocols, where the system is driven at a constant angular velocity?

1.2.1 Structure of ATP synthase

Here we summarize structural information presented mainly in [8, 27]. The comprehensive structure of the ATP synthase is quite complicated, but one can decompose it into two separate regions, the F_1 and the F_o regions, and each region can be decomposed further into its detailed constitutive subunits (Fig. 1.1). The structural dynamics can be summarized as a rotor-stator system: the central crankshaft (rotor) rotates thorough the central cavity of the ring structure (stator).

The F_1 region is composed of five different polymer chains, (in order of decreasing size of subunits) as α_3, β_3, γ, δ, and ϵ, which together are generally responsible for catalyzing the three steps of the overall chemical reaction converting between ATP and ADP. This stator region is held fixed in the mitochondrial matrix by some mechanical connections. There are three separate α chains and three separate β chains, which altogether compose a hexamer, the $\alpha_3\beta_3$ ring structure. This hexamer's specialized task is to promote the three steps in

ATP synthesis that will be discussed in the following sections. Although α and β subunits can both bind ATP molecules, only β subunits are catalytically active, with the capability to chemically synthesize ATP.

The central crankshaft, the connection of the two separate regions, is formed by the γ and ϵ subunits. This elongated structure rotates in the inner hole of the ring formed by α and β subunits, and on its opposite end connects to the F_o region embedded in the inner mitochondrial membrane (Fig. 1.3). Details of the coupling between the central shaft and the F_o component are still open questions. Recent investigation suggests a torsional elasticity between the shaft and the c ring rather than a rigid coupling between the two elements [37]. The key role of the central crankshaft is to mechanically connect the F_o and the F_1 regions in a way that establishes a tight coupling between the proton flow in F_o and the chemical reaction in F_1. The central shaft interacts with the hexamer ring structure by perturbing the catalytic site conformations to stimulate ADP and P_i binding, ATP synthesis, and ATP release. Finally, the δ subunit holds the entire hexamer ring fixed through a rigid connection with the membrane-bound F_o region.

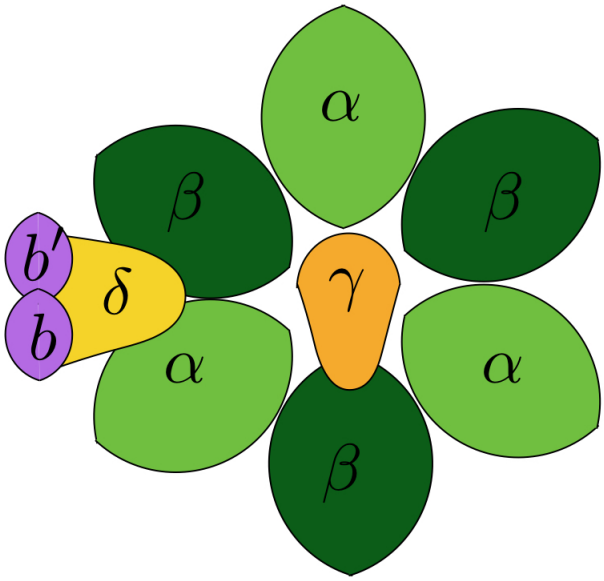

Figure 1.3: Schematic representation of the F_1 cross section. The central γ shaft rotates between the three α and three β subunits, thereby dynamically perturbing their conformational states. The b, b', and δ subunits fix F_1 within the mitochondrial matrix by forming a solid connection to the membrane.

Our primary focus is on the efficient driving of the detached F_1 region, but it is useful to have a general picture of the entire motor, here the entire F_oF_1 ATP synthase. The other main region, F_o, has a hydrophobic part forming a pathway for hydrogen ion translocation across the mitochondrial inner membrane and down the electrochemical gradient (established from the intramembrane space to the mitochondrial matrix by other machines). This

region is mainly composed of two types of polymer chains—∼10 c subunits (the exact number varies across different species) forming a ring and a single a subunit—which together form the proton tunnel across the membrane. The a subunit connects the c ring to the the F_1 region via the b and b' subunits and a single δ polymer chain (Fig 1.2). Thus the F_1 and F_o regions are tightly coupled to each other by two elongated arm structures: the rotor and the stator.

1.2.2 Mechanism of the catalytic region

Let us consider the mechanism by which ATP molecules are generally believed to be produced. The two constituent regions, F_1 and F_o, can be investigated separately. According to Boyer's classic model of rotary catalysis [26], the F_1 operation is summarized in three main steps. First, reactants including the ADP and the phosphate molecules bind. Second, the motor catalyzes the synthesis from them of ATP. Finally, ATP is released into the mitochondrial environment. The hexamer ring (shown in cross-section in Fig. 1.3 is composed of three α and three β subunits. The α subunits can bind ATP, but lack catalytic activity. Only the β subunits are catalytically active. Based on this hypothetical model that coarse-grains the chemical reaction progress into three intermediate steps, one can simply imagine three classes of conformations, which each β subunit can adopt (we ignore the step regarding the phosphate binding) according to the simplified three intermediate steps in the chemical-reaction coordinate. Essentially, the central crankshaft breaks the symmetry of the catalytic sites. As the central crankshaft rotates, it drives the interconversion of these three β subunit conformations, cycling between "open," "loose," and tightly "closed" states. The β subunit must be in the open state to permit ATP unbinding and subsequent reactant binding.

In the loose state, when ADP and phosphate are bound they are too distant to permit phosphate bond formation. Only in the tightly closed state are reactants brought sufficiently close to accomplish chemical synthesis.

1.2.3 Mechanically driven F_1

Various single-molecule experiments have been developed to perturb F_1 by forcing rotation of the central crankshaft. They typically attach a molecular or metallic handle, such as a fluorescent actin filament, gold nanobeads [28], a gold nanorod [29, 30, 31], polystyrene beads [32] or a magnetic bead [33, 34, 35, 36].

The F_1 ATPase can be experimentally detached from the rest of the entire ATP synthase motor and immobilized on a glass surface. A magnetic bead then can be attached to the central crankshaft. A rotating magnetic field forces the magnetic bead to rotate, in turn forcing rotation of the central crankshaft (Fig. 1.4). An indicator can be employed to indicate ADP-to-ATP chemical conversion, emitting a photon upon capture and hydrolysis

of ATP, so the number of emitted photons indicates the motor's ATP synthesis, and hence net cycles of rotation.

The central crankshaft radius has been estimated to be around ten nanometers [37], while the magnetic bead is typically micron-sized, so rotational diffusive motion is reasonably expected to be dominated by the magnetic bead's rotational diffusion.

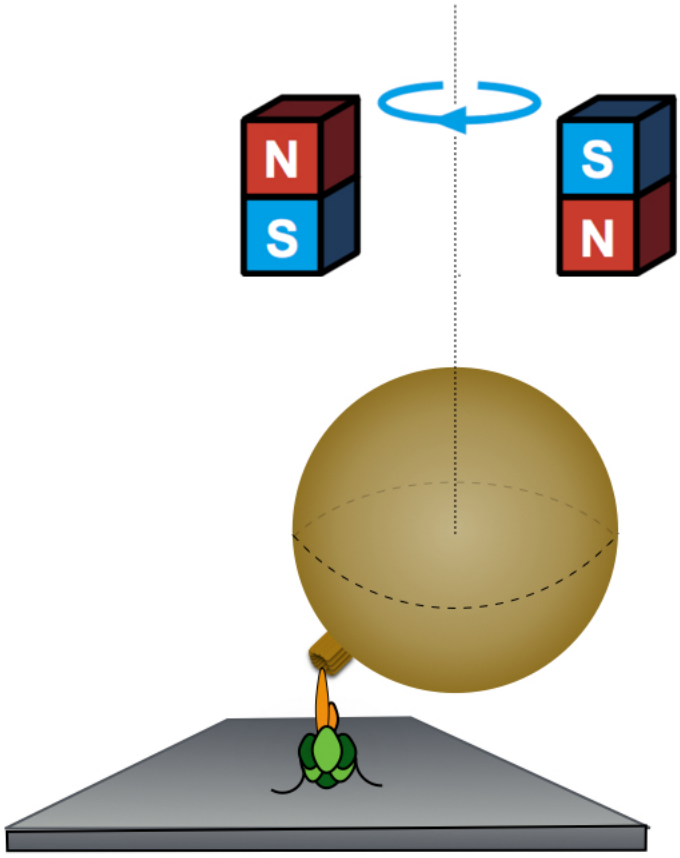

Figure 1.4: Schematic representation of the experimental set up for mechanically driving the F_1 ATP synthase. A magnetic bead is attached to the central shaft while F_1 is fixed over a surface. A rotational magnetic filed could be applied to force the system to rotate clockwise and anti-clockwise.

1.2.4 The protonmotive force

The F_o region couples proton flow to the mechanical rotation of the motor's central crankshaft. The F_o region is an integral membrane protein, it is relatively inaccessible experimentally, so the vast majority of recent research has studied the isolated F_1 region. Nevertheless, here

we summarize the proposed mechanism of proton flow across the membrane and its coupling to the F_1 catalytic process. In other words, how do the three catalytic sites in the F_1 region respond to the flow of hydrogen ions through the F_o proton channel? This requires examining the structure and operation of F_o. F_o is thought to be two types of polymers that create this molecular complex including multiple *c* subunits collectively forming a ring structure, as well as a single *a* subunit, which is connected to the external surface of the *c* ring (Fig. 1.2).

An elegant mechanism has been proposed to describe the proton flow [46]. Hydrogen ions transfer through the F_o proton pathway, forcing the *c* ring to rotate in one direction and the central crankshaft rotor to rotate in the opposite direction, ultimately stimulating ATP production in the catalytic sites of the F_1 region. Based on experimental evidence, the *a* subunit has been proposed to consist of two hydrophilic half channels (neither of which spans the entire membrane alone), one open towards the matrix environment and the other open to the intermembrane area [47]. These channels guide and conduct the proton from the high concentration area towards the low concentration area across the mitochondrial inner membrane. A negatively charged residue in the center of each *c* subunit is responsible for pulling positively charged protons toward the transfer tunnel, from the region with high ionic concentration.

The proton transfer mechanism can be summarized in a few general steps [46, 48]. First, the hydrophilic half channel is open to the matrix. At the middle point of the half channel is the *c* subunit's negatively charged residue, which draws a proton into the channel from the high ion concentration in solution (Fig. 1.5). When the hydrogen ion binds to the residue, the resulting product is more hydrophobic, so it naturally relocates to the hydrophobic environment of the inner membrane interior. When this particular *c* subunit rotates, it forces the ring structure to rotate until a *c* subunit, with negative charge at the center, faces the half channel that in turn faces the mitochondrial matrix, the low concentration region. Finally, the proton is released into the matrix. This proton flow from high concentration to low concentration powers the rotation of the ring, which ultimately stimulates the catalytic reactions in the F_1 region by the rotation of the central crankshaft.

The *c* ring is composed of a different number of *c* subunits in different organisms [49]. Given the hypothesized tight coupling between proton flow and ATP production, it is thought that the number of *c* subunits in the ring structure equals the 'gearing ratio,' the number of protons transported per one cycle of the *c* ring rotation, and hence per one rotational cycle of F_1 synthesizing three ATP molecules. This gearing ratio is correlated across organisms with the actual protonmotive force across the inner mitochondrial membrane [49], suggesting that the gearing ratio could have been evolutionary tuned to provide the minimum driving force necessary to synthesize ATP, and hence achieve much higher efficiency during the system operation.

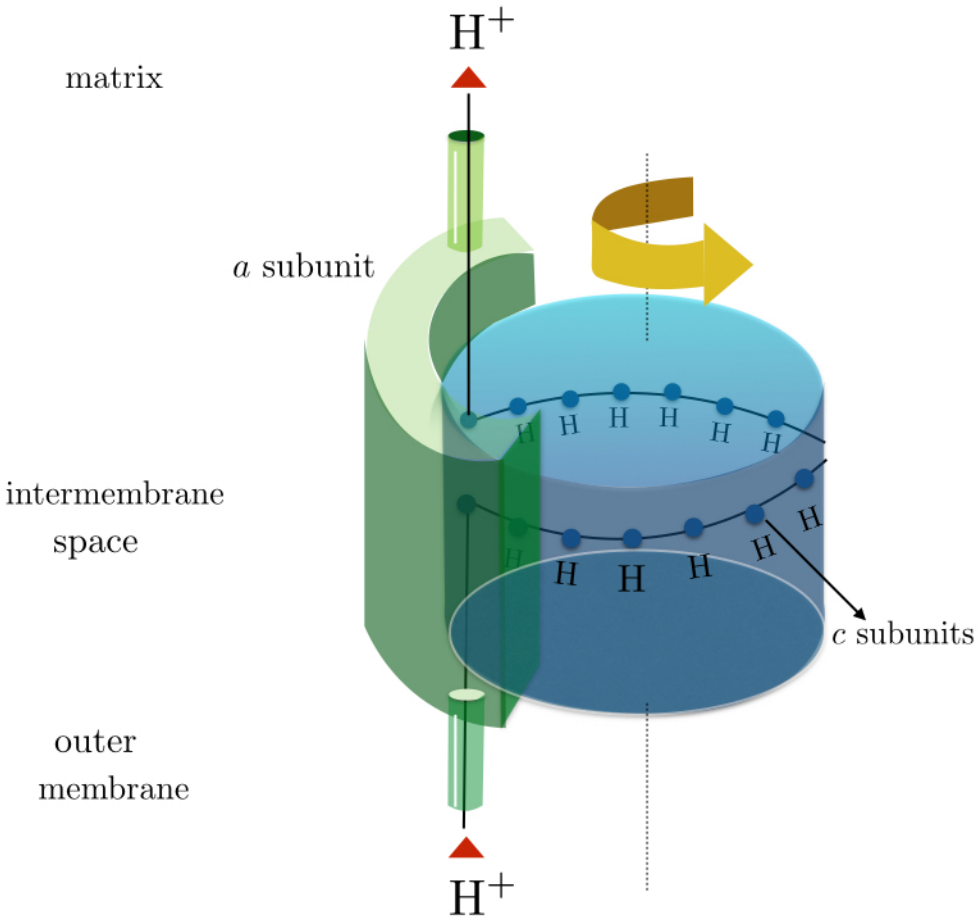

Figure 1.5: Schematic hypothetical representation of the isolated F_o region. Protons (labeled by 'H') bind the c subunits. This binding forces the c ring to rotate which ultimately rotates the central shaft.

1.3 Summary

In summary, there is an interest in characterizing optimal (minimum-dissipation) driving protocols of F_1 ATP synthase, because of the recent experimental evidences indicating a remarkably high efficiency for the operation of this rotary mechanochemical molecular motor.

For this purpose, in the next chapters of this thesis, we will first summarize an approximate linear-response theoretical framework [17], and then, based on basic experimental findings regarding the structure and dynamics of the F_1 ATP synthase (discussed in Chapter 3), we introduce a simplified thermodynamic model system representing the isolated F_1 ATP synthase with the minimal resolution required to capture some of the system's interesting properties. In the results chapter, we will present optimal driving protocols across

control parameter space, and examine their dependence on external driving strength and internal model parameters. We also examine how energetically effective are such optimal driving protocols compared to naive (constant velocity) protocols, quantifying how much energy is saved.

Chapter 2

Theoretical Framework

Classical thermodynamics is naturally limited in its applicable regime to describe many different classes of physical phenomenon. It is essentially a mathematical framework for describing physical systems in equilibrium, where thermodynamic systems can be characterized by the Gibbs-Boltzmann probability distribution [50, 51]. The theory of linear response provides a framework for describing near equilibrium properties of physical systems, where equilibrium departures arise from a weak external perturbation [52]. Nevertheless, many everyday physical processes occur far from equilibrium, where the linear-response approximation may no longer be accurate enough because perturbations could in general be both strong and fast-varying. Nature, for instance, is a collection of a wide variety of interacting open systems that, when driven by the continuous flow of matter and energy, are intuitively expected to be far from equilibrium. In this regard, living organisms are inherently open interacting systems that often operate rapidly, and thus they are expected to be out of equilibrium, and typically require a non-linear description.

Therefore, it would be greatly useful to develop methods and frameworks by which out of equilibrium processes could be comprehended in general. A primary application of such theoretical frameworks would be a deeper investigation on nonequilibrium physical processes in different areas of science such as processes in living organisms, or even driven quantum systems near or far from equilibrium. In this research project, we focus on the nonequilibrium driving protocols externally perturbing a rotary mechanochemical molecular motor embedded in an extremely noisy environment such as the cellular milieu.

2.1 Nonequilibrium thermodynamics

During recent decades, new approaches have been developed to classify general laws that describe physical systems in the nonequilibrium thermodynamic regime. For example, an equality has been introduced that establishes a general connection between the free energy difference of two equilibrium states, and the average work required to push such a system

between the two equilibrium states via a nonequilibrium finite-time driving protocol [54, 55]. Further major progress came from comparing probability distributions of the work that is required during a particular nonequilibrium driving protocol with that during its 'time-reversed' driving protocol. This nonequilibrium fluctuation theorem states that, assuming microscopic reversibility, the likelihood ratio of the forward-time trajectory and its time reversal is exponential in the entropy produced (or equivalently in our example the energy dissipated) during the forward trajectory [56, 57].

Biological systems and in particular molecular motors operate in finite-time cycles out of equilibrium, and in general dissipate energy in the course of their function. A central question is how they can function effectively at minimum energetic cost. We lack a comprehensive answer to this broad question, but for systems operating near equilibrium, a general characterization of optimal (minimum-dissipation) driving protocols was recently developed [17]. The key quantity in this description is the time integral of the force autocorrelation function, which we discuss in more detail in the next few sections. We apply this linear-response approximation to our thermodynamic system in order to calculate optimal driving protocols for externally perturbing a model of the stochastic rotary mechanochemical motor protein F_1 ATP synthase.

2.2 Dissipation near equilibrium

This section summarizes the central derivation of the nonequilibrium optimal protocols as described in [17]. A thermodynamic system can in general exchange energy with its environment by performing or receiving work, or by transferring heat, across its physical boundaries. In general, thermodynamic systems can be described by internal system coordinates $\vec{x}$ specifying a particular system microstate, and external control parameters $\vec{\lambda}$, a set of canonical coordinates describing the external environmental interactions with the system. Control parameters could include external forces exerted by external agents, or even temperature of the surrounding thermal bath.

Physical properties of thermodynamic systems, such as the internal energy $U(\vec{x}, \vec{\lambda})$, are determined by the state of both internal and external parameters. For instance, for a system in contact with an electric or a magnetic field, external parameters could be the field spatial orientation and its magnitude, which can be quantified by consideration of the position and charge distribution of external agents, for example permanent magnets. On the other hand, the electrical or chemical state of the molecules composing the system can be considered as the internal parameters describing the system's state.

In general, a thermodynamic system left in contact with a heat reservoir at constant temperature will ultimately reach equilibrium in the long time limit. The system can in general occupy many microstates with various energy levels, so at equilibrium the canonical

ensemble specifies an energy-based probability for occupying each of the possible states [50]:

$$p(\vec{x} \mid \vec{\lambda}) = Z^{-1} \exp[-\beta U(\vec{x}, \vec{\lambda})], \tag{2.1}$$

where $Z = \sum_{\vec{x}_i} \exp[-\beta(U(\vec{x}_i, \vec{\lambda})]$ is the canonical partition function, and $\beta \equiv 1/(k_B T)$ is proportional to the inverse of temperature.

Consider a thermodynamic system initially thermally equilibrated with the thermal bath, but then subject to a time-dependent driving protocol between specified initial and final control parameter values. As a result of such external time-dependent perturbation, the system is driven out of equilibrium. During the protocol, the system absorbs (or gives off) heat to gradually relax toward a new equilibrium distribution characterized by the new state of the external control parameters. Such a process pushing the system to a new macrostate in parameter space requires doing/receiving some quantity of work W. At the end of the process (protocol), the external control parameter can be kept constant in time, letting the system fully equilibrate.

The second law of thermodynamics asserts that the work exerted by the external agents during the previous process must equal or exceed the equilibrium free energy difference ΔF between the initial and final equilibrium states:

$$W \geq F_2 - F_1, \tag{2.2}$$

where the equality holds if the process occurs reversibly (infinitely slowly). This inequality can be recast as the Clausius inequality: $\Delta S \geq \frac{Q}{T}$, where Q and S are heat and entropy, respectively.

The internal energy change of our thermodynamic system is described by the first law of thermodynamics

$$\Delta U = Q + W. \tag{2.3}$$

Work is associated with system energy changes due to variation of external control parameters during the work steps, whereas heat is associated with energy changes due to transition between different microstates $\vec{x}$ during the relaxation steps.

Although the internal energy U is a state function, both transferred heat and exerted work on the system are naturally trajectory dependent. The average power flow across the system boundaries is the rate of work done by external agents. Following from the first law of thermodynamics, the average instantaneous rate of energy flow into the system, $\frac{\mathrm{d}\langle U \rangle_{\mathbf{\Lambda}}}{\mathrm{d}t}$, is the average sum of the instantaneous rate of heat flow $\mathrm{d}Q/\mathrm{d}t$ and the instantaneous power

$P \equiv \mathrm{d}W/\mathrm{d}t$ due to changing control parameter during the protocol:

$$\frac{\mathrm{d}\langle Q\rangle_{\mathbf{\Lambda}}}{\mathrm{d}t} \equiv \left\langle \frac{\mathrm{d}x}{\mathrm{d}t}\frac{\partial U}{\partial x} \right\rangle_{\mathbf{\Lambda}} \tag{2.4}$$

$$P \equiv \frac{\mathrm{d}\langle W\rangle_{\mathbf{\Lambda}}}{\mathrm{d}t} \equiv -\frac{\mathrm{d}\lambda}{\mathrm{d}t}\left\langle -\frac{\partial U}{\partial \lambda} \right\rangle_{\mathbf{\Lambda}}, \tag{2.5}$$

where negative derivatives of the system energy with respect to control parameters $X \equiv -\frac{\partial U}{\partial \lambda}$ are generalized (conjugate) forces. Angled brackets with subscript $\mathbf{\Lambda}$ indicate a nonequilibrium ensemble average under the time-dependent control protocol $\mathbf{\Lambda}$. The time derivative of the control parameter can be brought out of the average because it proceeds based on a deterministic time-dependent protocol. This microscopic definition of work is discussed in more detail in [58, 59].

A system in equilibrium with a thermal bath and current state of control parameter at time t_0 experiences an average power

$$P(t_0) = -\frac{\mathrm{d}\lambda(t_0)}{\mathrm{d}t}\langle X\rangle_{\lambda_{(t_0)}}, \tag{2.6}$$

where angled brackets with subscript $\lambda_{(t_0)}$ indicate an equilibrium ensemble average at fixed control parameter $\lambda_{(t_0)}$.

Therefore, in a system driven out of equilibrium according to a nonequilibrium time-dependent protocol, the average excess power is

$$P_{\mathrm{ex}}(t_0) = -\frac{\mathrm{d}\lambda(t_0)}{\mathrm{d}t}\langle \Delta X(t_0)\rangle_{\Lambda}, \tag{2.7}$$

where $\Delta X(t_0) \equiv X(t_0) - \langle X\rangle_{\lambda_{(t_0)}}$ is the deviation of the conjugate force X at time t_0 from its corresponding equilibrium average given fixed control parameter $\lambda(t_0)$, and angled brackets with subscript Λ indicate an average over the nonequilibrium protocol Λ.

Based on the theory of linear response, the departure of the system's response from that of the unperturbed system can be expressed as a time integral of the perturbation exerted by the external agents. In general, the system response can be expanded into a Taylor series including terms involving different powers of the external perturbation. The first-order term expresses the system response to linear order in the external conjugate forces.

Dynamic linear response theory can determine the ensemble and time-average of dynamical variables in response to such external manipulation [52]:

$$\langle X(t_0)\rangle_{\Lambda} = \int_{-\infty}^{t_0} \mathrm{d}t' \chi(t_0 - t')[\lambda(t') - \lambda(t_0)] \tag{2.8}$$

$$\chi(t) = -\beta\theta(t)\frac{\mathrm{d}}{\mathrm{d}t}\langle \delta X(0)\delta X(t)\rangle_{\lambda(t_0)}, \tag{2.9}$$

where $\chi_{ij}(t)$ is the response function of the conjugate force X_j at time t to the perturbation in control parameter λ_i at time zero [51], $\theta(t) = 1, t > 0; 0, t \leq 0$ is the Heaviside function, and $\beta = 1/(k_{\mathrm{B}}T)$.

If the external control parameter varies infinitely slowly, then the system relaxes back to equilibrium rapidly compared to the protocol timescale. On the other hand, if the control parameters change rapidly, the system does not have enough time to fully relax given the new control parameter value, and basically lags behind the control parameter protocol. This class of operations is irreversible.

The linear response approximation assumes a sufficiently slow protocol Λ such that the nonequilibrium response can be considered as a linear function of control parameter variation, and higher order terms are assumed to be negligible.

Substituting Eq. (2.8), describing the near-equilibrium deviation of conjugate forces, into Eq. (2.7), gives the excess power in the linear-response approximation

$$P_{\mathrm{ex}}(t_0) = \beta \frac{\mathrm{d}\lambda}{\mathrm{d}t} \int_{-\infty}^{t_0} \mathrm{d}t' \frac{\mathrm{d}\langle \delta X(0) \delta X(t') \rangle_{\lambda(t_0)}}{\mathrm{d}t'} (\lambda(t_0) - \lambda(t')) \ . \tag{2.10}$$

The time derivative of the force autocorrelation function can be further simplified by the method of integration by parts. Multiple terms vanish due to the boundary conditions at $t' \to -\infty$ and $t' \to t_0$. The boundary terms in fact make no significant contribution, since all measurements separated by a very long time interval are intuitively expected to be uncorrelated. These simplifications produce the central equation characterizing excess power of our thermodynamic system near equilibrium distribution,

$$P_{\mathrm{ex}}(t_0) = \beta \frac{\mathrm{d}\lambda(t_0)}{\mathrm{d}t} \int_0^{\infty} \mathrm{d}t'' \Sigma^{\lambda(t_0)}(t'') \frac{\mathrm{d}\lambda(t_0)}{\mathrm{d}t} \tag{2.11}$$

$$P_{\mathrm{ex}}(t_0) = \beta \left[\frac{\mathrm{d}\lambda}{\mathrm{d}t}\right]_{t_0} \zeta(\lambda(t_0)) \left[\frac{\mathrm{d}\lambda}{\mathrm{d}t}\right]_{t_0} \ . \tag{2.12}$$

Here, $\Sigma^{\lambda(t_0)}(t'')$ is the covariance for conjugate force X separated by time t'', at constant control parameter $\lambda(t_0)$.

This analysis collapses the integral of the time-dependent covariance matrix into a time-independent equilibrium matrix, a generalized friction tensor:

$$\zeta(\lambda(t_0)) = \beta \int_0^{\infty} \mathrm{d}t'' \langle \delta X(0) \delta X(t'') \rangle_{\lambda(t_0)} \ . \tag{2.13}$$

In conclusion, nonequilibrium excess power P_{ex} can be approximated in the regime of sufficiently slow driving protocols. This linear-response approximation is based on determination of the time-integrated autocorrelation function of the system's conjugate forces. This expression is interesting because it is in general fully local, depending only on the current value of the system control parameter and its time derivative. This expression is in appar-

ent contrast with the general picture of an out-of-equilibrium physical process, where all physical observables are expected to depend on the entire history of the driving protocol.

In general, correlation functions for a physical system are measurements of order: they describe how different variables, such as spin, density, or force, are related at different positions and/or times. In our model system, the force autocorrelation function describes how the conjugate force at different times is correlated: it quantifies how deviations of the conjugate force from the average persist over time. Thus, the time evolution of a correlation function can be interpreted as the system forgetting its initial state. The correlation function is naturally maximized at zero time separation $t' = 0$, while in the long time limit, the function decays to negligible values, and the system becomes uncorrelated with its previous state (forgets the past). The error in approximating the infinite time integral of a correlation function with its integral over finite time increases in slow relaxing correlation functions, but we choose vary the cutoff time to keep relative error constant.

A recent derivation [60, 61] simplifies the friction coefficient description for a broad class of over-damped dynamics, where systems are assumed to diffuse in one physical dimension x:

$$\zeta_{\mathrm{ij}}(\lambda) = \frac{1}{D}\int_{-\infty}^{+\infty} \mathrm{d}x \left[\frac{\partial_{\lambda^i}\Pi_{\mathrm{eq}}(x,\lambda)\partial_{\lambda^j}\Pi_{\mathrm{eq}}(x,\lambda)}{\rho_{\mathrm{eq}}(x,\lambda)}\right], \tag{2.14}$$

where D is the system diffusion coefficient, $\rho_{\mathrm{eq}}(x,\lambda)$ is the equilibrium probability distribution over the system's microstates and $\Pi_{\mathrm{eq}}(x,\lambda)$ is the cumulative distribution function. This new expression for the friction coefficient requires only the equilibrium probability distribution of the thermodynamic system and the system diffusion coefficient. This expression considerably reduces the significant time that is usually required for calculating the time integral of the force-force autocorrelation function (especially when the correlation function relaxes slowly) because it only depends on the equilibrium cumulative probability distribution.

However, there are some restrictive assumptions in the derivation of this simple expression, which limit its applicability. For example, the system potential energy must satisfy $U(x,\lambda) \to \infty$ as $|x| \to \infty$. In general, this expression seems to be an appropriate description, when stochastic equation of motion is linear or simply the imposed potential is a harmonic potential (linear force). On a more general energy landscape, this derivation breaks down, and thus different methods must be used to reduce the computational time required to calculate the generalized friction coefficient in Eq.(2.13).

To provide further physical intuition, we note that the generalized friction coefficient can be decomposed into two components

$$\zeta(\lambda(t)) = k_{\mathrm{B}}T\ \tau(\lambda(t))\ I(\lambda(t))\ , \tag{2.15}$$

the integral relaxation time $\tau(\lambda(t))$ and the force variance (by definition equals the Fisher information in the context of information theory) $I(\lambda(t))$ [40]), defined in equilibrium as

$$\begin{aligned} I(\lambda) &= \sum_n p_{\mathrm{n}} \left(\frac{\partial \ln p_n}{\partial \lambda} \right) \left(\frac{\partial \ln p_n}{\partial \lambda} \right) \\ &= \left\langle \delta X^2 \right\rangle_\lambda \ . \end{aligned} \tag{2.16}$$

Here the sum is over the system microstates. In the canonical ensemble, the Fisher information with respect to the external control parameter is the covariance matrix of fluctuations around equilibrium. In other words, Fisher information of a thermodynamic system expresses the size of thermal fluctuations at equilibrium [43]. Fisher information is also insightful in the field of information/thermodynamic geometry. The Fisher information matrix (when we have a multidimensional control parameter) is a covariance matrix, which by definition is symmetric and positive semi-definite (all the eigenvalues are positive). Thus it can be used as a metric to quantify the distance between a pair of points in the control parameter space [44].

The integral relaxation time is

$$\tau = \int_0^\infty \mathrm{d}t' \frac{\left\langle \delta X(t') \delta X(0) \right\rangle_\lambda}{\left\langle \delta X^2 \right\rangle_\lambda} \ . \tag{2.17}$$

This derivation was for systems that relax to an equilibrium distribution. Recent work has shown that this framework, with a couple of extra assumptions, is also applicable for slow transitions between nonequilibrium steady states (NESS) [12], that could in general be arbitrarily far from equilibrium. An important feature of NESS is that detailed balance is broken, which in fact requires constant dissipation of energy. In our probabilistic picture, in an NESS distribution, due to the constant flow of probability across the system boundaries, the system naturally dissipates heat on an ongoing basis, known as the housekeeping heat [69]. This constant (on average) heat transfer between the thermodynamic system and the thermal bath is necessary to maintain the system in a particular steady-state distribution. The excess heat is then the difference between the total dissipated heat and the necessary housekeeping heat.

In this regime, elements of the friction tensor are given by the time integral of the conjugate-force autocorrelation function in the nonequilibrium steady state ensemble rather than in equilibrium. This generalization establishes a connection between excess work and stationary thermal fluctuations in a nonequilibrium steady state. Moreover, at nonequilibrium steady state the appropriate conjugate forces are not determined by the current microstate and control parameter values, but rather depend on the stationary distribution

over microstates, and hence on the full system dynamics. Furthermore, this generalization only provides a lower bound (not an equality) for the energetic inefficiency.

Dynamics of our system is governed by a master equation. Thus, the nonequilbrium steady state distribution can be determined numerically by solving $\hat{T} \cdot p_{\rm ss}^{\rm noneq} = 0$, where $\hat{T}$ is the transition rate matrix and $p_{\rm ss}^{\rm noneq}$ is the nonequilibrium steady-state probability distribution. More details on implementing the master equation is provided in the next two chapters. Similar to the previous near-equilibrium picture, we start from a NESS distribution rather than an equilibrium distribution, and by varying the control parameter in a time-dependent manner, we do work on the system and drive its distribution away from NESS. At the end of the protocol, we have a nonequilibrium probability distribution that could be far away from equilibrium/NESS distribution, but at fixed final control parameter the distribution will eventually relax to a NESS distribution.

2.3 Optimal protocol description

For a physical system proceeding according to an externally controlled time-dependent driving protocol $\lambda(t)$, the optimal driving protocol is the one that minimizes the average work required to transit, in a given finite-time interval, between the two points given in the control parameter space. Consider an out-of-equilibrium physical process, where our system is prepared in an equilibrium thermodynamic state, then is driven out of the equilibrium state by variation of the external control parameters. A quantity of work W is imposed on the system by the nonequilibrium time-dependent driving protocol. Repeating this experiment many times, always starting from the same equilibrium state and enacting the same driving protocol, produces a different W each time, due to the stochastic system fluctuations. The final result is a work distribution for driving the system between the two particular points in control parameter space. According to the Clausius inequality, the average work exceeds the equilibrium free energy difference between the two equilibrium states of the thermodynamic system,

$$\langle W \rangle \geq \Delta F \ . \tag{2.18}$$

One might encounter an unexpected rare realization of the experiment, where W is less than the free energy difference. These so-called violations of the second law of thermodynamics are relatively rare random events, and the Clausius inequality still holds on average. Equality (work equals equilibrium free energy) is obtained when the control protocol is infinitely slow, however when the time allotted for the driving protocol is finite, the mean work will be larger. But what is the minimum work for a given allotted time and control parameter endpoints?

Characterizing optimal protocols would enable the extraction of maximal work from a given free energy difference during a particular finite-time driving protocol. Optimal nonequilibrium driving protocols have been investigated in different regimes of parameter space as well as in different thermodynamic systems [16, 62, 63], such as a stochastic particle dragged by an optical tweezer with a harmonic potential, or held in a fixed quadratic trap with a time-dependent strength. Optimal driving protocols have also been found for a colloidal Brownian particle coupled to an optical trap and a tilted external ratchet potential, as well as a Brownian particle in a double well potential [64].

The dissipation of a slow driving protocol can be minimized by minimizing the finite-time integral of the excess power, giving the mean excess work

$$W_{\rm ex}(t_0) = \int_0^{t_0} {\rm d}t \; P_{\rm ex}(t, \lambda(t), \dot{\lambda}(t)) \; . \tag{2.19}$$

This represents the difference between the mean work invested in the system in the finite-time, but sufficiently slow, protocol, and the work required if the system were always equilibrated during the protocol.

For systems with a single control parameter, the time integral of excess power is minimized by solving an Euler-Lagrange equation [17, 65]:

$$\frac{\partial L(t, q, \dot{q})}{\partial q} = \frac{\rm d}{{\rm d}t}\left[\frac{\partial L(t, q, \dot{q})}{\partial \dot{q}}\right] \; . \tag{2.20}$$

A control parameter protocol Λ giving a stationary value (a local minimum, maximum, or saddle point) for the total excess work $W_{\rm ex}(t_0)$ will satisfy the Euler-Lagrange equation with excess power substituted for L:

$$0 = -\frac{\rm d}{{\rm d}t}\left[\frac{\partial P_{\rm ex}(t, \lambda(t), \dot{\lambda}(t))}{\partial \dot{\lambda}(t)}\right] + \left[\frac{\partial P_{\rm ex}(t, \lambda(t), \dot{\lambda}(t))}{\partial \lambda(t)}\right] \tag{2.21}$$

$$= -\frac{\partial \zeta(\lambda(t))}{\partial \lambda}\dot{\lambda}^2(t) - 2\zeta(\lambda(t))\ddot{\lambda}(t) \; . \tag{2.22}$$

For more details on this derivation see [17]. The above criteria for characterizing stationary results is satisfied when the time derivative of the control parameter, the velocity of driving protocols $\dot{\lambda}(t)$, is proportional to the inverse square root of the generalized friction coefficient, $\zeta(\lambda)^{-1/2}$:

$$2\zeta\partial_t(\zeta^{-1/2}) + \partial_\lambda(\zeta)[\zeta^{-(1/2)}]^2 = 2\zeta\dot{\lambda}\partial_\lambda(\zeta^{-1/2}) + \partial_\lambda(\zeta)\zeta^{-1} \tag{2.23}$$

$$= 2\zeta\zeta^{-1/2}\left(\frac{-1}{2}\right)\zeta^{-3/2}\partial_\lambda(\zeta) + \partial_\lambda(\zeta)\zeta^{-1} \tag{2.24}$$

$$= 0 \; . \tag{2.25}$$

In conclusion, the optimal, minimum-dissipation, driving protocols for a thermodynamic system with only one active control parameter obey

$$\dot{\lambda}^{\mathrm{opt}}(t) \propto \zeta(\lambda(t))^{-(1/2)} \ . \tag{2.26}$$

Substituting Eq. (2.26) into Eq. (2.12) shows that excess power on an optimal driving protocol is a constant value during the course of the driving process. This optimal driving protocol proceeds slowly where the system shows large resistance (high friction coefficient) against rapid changes of the external control parameters (typically near energy barriers). On the other hand, the optimal driving protocol proceeds rapidly for small resistance (low friction coefficient), generally near thermodynamic metastable states. In general, according to Eq. (2.12), excess power scales as the square of the control parameter velocity, $\left(\frac{\mathrm{d}\lambda}{\mathrm{d}t}\right)^2$, while for an optimal driving protocol between two specified points in the control parameter space, the total excess work scales linearly with control parameter velocity, namely with $\left|\frac{\mathrm{d}\lambda}{\mathrm{d}t}\right|$.

Some of this extra work will be dissipated as heat across the system boundary to the environment, and the remaining extra energy is stored in the system, as an extra energy associated with being away from equilibrium. Once the system completely relaxes to the final equilibrium distribution, then all the extra energy has dissipated to the environment, and hence the excess work exactly equals the total dissipation.

Now that we are equipped with an approximate theoretical framework—near equilibrium and near nonequilibrium steady state—for characterizing the optimal driving protocols, and are also familiarized with the general properties, functions and structure of F_1 ATP synthase, we will introduce in the next chapter a simple model of a stochastic rotary mechanochemical molecular motor, inspired by F_1 ATP synthase. In particular, we will apply this mathematical framework to our thermodynamic model system to determine the generalized friction coefficient, optimal driving velocities, and finally the optimal driving protocols on a periodic energy landscape.

Chapter 3

Model System

A thermodynamic model system that captures the general properties and behaviour of the F_1 ATP synthase is essential for the preliminary investigation on this motor's optimal driving protocols. This model must incorporate stochastic dynamics arising from thermal fluctuations, in this case rotational diffusion in both energetically favorable and unfavorable directions, here clockwise and anticlockwise rotations [66].

This model should also include the hypothesized tight coupling between mechanics and chemistry such that chemical reaction progress strongly depends on mechanical rotation. For simplicity we assume that F_1 must convert three molecules of ATP to be able to mechanically rotate one full cycle; conversely, to convert three molecules of ATP, it must mechanically rotate a full cycle.

It has also been experimentally verified that the central crankshaft rotates roughly between only three rotational angles, corresponding to pointing at each of the three catalytic β subunits [9], such that in each mechanical step it rotates $\sim 120^o$ degrees to the next catalytic site. Incorporating only these features, the thermodynamic model system that we introduce and study here can generally represent a broad class of stochastic rotary motors, coupling mechanical rotation to progress in specific chemical reactions.

In the specific case of F_1 ATP synthase, the chemical reaction is the reaction of producing ATP molecules from ADP molecules, believed to be stimulated by releasing or binding a phosphate molecule at a β subunit. We model a simplified version of this reaction (ignoring the intermediate step for binding the phosphate group) through two states with different energy levels at a given rotational angle of the magnetic trap (representing the reactant and the product) of the crankshaft (Fig. 3.1).

Transition dynamics between such two states is generally regulated by the height of an energy barrier between the two states. We also model an external, time-dependent, driving force in the form of a rotating magnetic trap, represented by a sinusoidal potential. The magnetic trap drives our system out of equilibrium according to a deterministic rotation

schedule $\theta_0(t)$ for the preferred magnetic bead orientation (orientation of the magnetic trap) θ_0 (corresponding to the minimum of a periodic potential).

The magnetic field pushes the bead, which rotates in response to this external perturbation and is tightly attached to the central crankshaft. In summary, we formulate a cyclic six-state model system, with states A through F arrayed on a ring, in accordance with the schematic representation of the top view of the F_1 ATP synthase (Fig. 1.3).

3.1 Model Representation

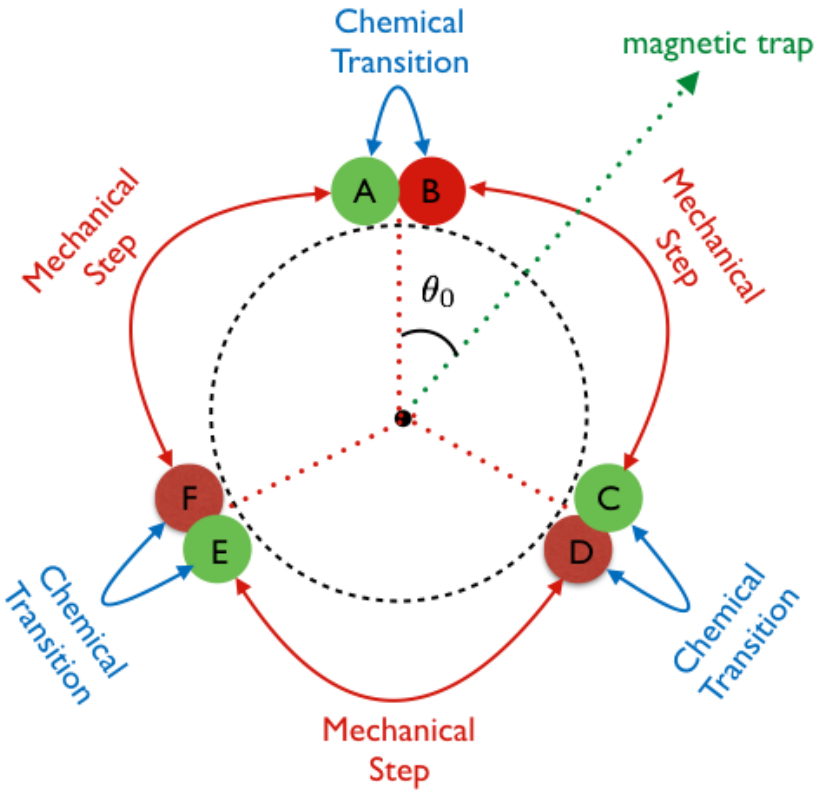

Figure 3.1: A simple thermodynamic model for the F_1 ATP synthase in the presence of external perturbation.
States A and B, C and D, and E and F have angular locations zero, $\frac{2\pi}{3}$, and $\frac{4\pi}{3}$, respectively. Mechanical transitions correspond to crankshaft rotation, and chemical transitions correspond to conversion between ATP and ADP molecules. There are mechanical energy barriers halfway between the states, namely at $\frac{\pi}{3}$, $\frac{3\pi}{3}$, and $\frac{5\pi}{3}$, as well as chemical reaction energy barriers at zero, $\frac{2\pi}{3}$, and $\frac{4\pi}{3}$. The magnetic trap is parameterized by the angular orientation of the trap minimum θ_0 relative to the location of states A and B at zero degrees.

In the schematic representation of our model system (Fig. 3.1), states A and B sit at zero, C and D at $\frac{2\pi}{3}$, and E and F at $\frac{4\pi}{3}$. Transitions from A to B, C to D, and E to F involve the synthesis of ATP, while the reverse reactions decompose ATP to ADP and

phosphate (the chemical reaction is microscopically reversible). No mechanical reorientation of the central crankshaft occurs during these transitions. On the other hand, transitions between F and A, B and C, and D and E represent mechanical rotation of the central shaft through $\frac{2\pi}{3}$ and does not involve any chemical reaction.

Due to the tight coupling between chemistry and mechanics, there are no straight transitions between non-adjacent states, so during a complete cycle of the motor (a 2π rotation of the central crankshaft), the system always produces three ATP molecules from ADP molecules or in the reverse direction decomposes three ATP to ADP molecules. We consider the case of strong coupling between the magnetic field and magnetic bead. In the limit of strong magnetic fields and a slow driving protocol, the motor is expected to rotate along with the magnetic field. However, in a weak magnetic field or during fast driving protocols, the motor (central crankshaft along with the magnetic bead), is expected to lag behind the magnetic field's time-dependent orientation, $\theta_0(t)$.

3.2 System dynamics

Dynamics of the system can be analyzed through the system's stochastic exploration of the energy landscape. Transition state theory [52] provides a theoretical framework to estimate transition rates of a stochastic object crossing an energy barrier.

In general, when thermal fluctuations are small compared with the height of the energy barriers, a stochastic particle is trapped strongly in its local potential well, diffusing for a significant period of time within the well, before ultimately getting kicked over the energy barrier. When temperature is low enough to be in this weak thermal fluctuation limit, the equation of motion can produce transmission rates that depend on a (near-)equilibrium probability distribution within the local well. According to transition state theory, crossing rates are proportional to the exponentiated free energy differences between the metastable state (local potential minimum) and the energy barrier. This framework should be an acceptable approximation in a high friction environment for the system's potentially complicated diffusion. If the environment does not provide enough friction then more complicated dynamical considerations must be taken into account to calculate reasonable crossing rates [53].

Generally, external perturbation of the energy landscape is imposed by changing the magnetic trap angular orientation and strength according to a time-dependent driving protocol. For this purpose, we model an additional periodic potential with minimum located at θ_0 and spring constant (trap stiffness-magnitude of the externally imposed potential) k.

The spring constant k can in principle be controlled externally by the experimentalist, but in this work we limit our attention to the trap minimum θ_0, which in the schematic representation of the model system (Fig. 3.1) is a green vector with angular orientation θ_0 relative to the angle of states A and B.

We assume that our system is fully embedded in a medium with a fixed chemical potential difference of ATP and ADP molecules, such that ongoing chemical reactions insignificantly influence concentration of the molecules around the system. In other words, concentrations of molecules are assumed to be recovered significantly faster than the system progress in chemical reactions.

We define a six-dimensional probability vector representing the system's probability distribution, $\vec{p} = (p_{\mathrm{A}}, p_{\mathrm{B}}, p_{\mathrm{C}}, p_{\mathrm{D}}, p_{\mathrm{E}}, p_{\mathrm{F}})$. Due to the variation of the control parameters, the probability distribution is in general a function of time, and here we observe its time-dependence evolution through a master equation:

$$\frac{\mathrm{d}\vec{p}}{\mathrm{d}t} = \hat{T} \cdot \vec{p}\,, \tag{3.1}$$

where $\hat{T}$ is a tridiagonal 6×6 transition rate matrix representing the system's diffusive dynamics. For $i \neq j$, the matrix element $T_{i,j}$ is the probability per unit time for a system in state i to make a transition to state j.

The diagonal elements of T are negative and are determined by conservation of probability. In general, transition rates are determined according to transition state theory, where matrix elements could have both zero and nonzero off-diagonal entries based on the collective effects of the unperturbed energy landscape and the sinusoidal external potential:

$$\begin{aligned} T_{i,i+1} &\propto \exp\{-\beta[E^{\ddagger}_{i,i+1}(k,\theta_0) - E_i(k,\theta_0)]\} \\ E_i(k,\theta_0) &= E_i - k\cos(\theta_i - \theta_0) \\ E^{\ddagger}_{i,i+1}(k,\theta_0) &= E^{\ddagger}_{i,i+1} - k\cos(\theta_{i,i+1} - \theta_0)\ . \end{aligned} \tag{3.2}$$

We have chosen a sinusoidal function because the energy function corresponding to the interaction of a magnetic dipole (here located within the magnetic bead) and a constant magnetic filed is similar to this mathematical form. Under these circumstances, Eq. (3.1) has a unique equilibrium (or nonequilibrium steady-state) solution, which we can denote by $\vec{p}_{\mathrm{eq}}$ (or $\vec{p}_{\mathrm{ss}}$), and any initial distribution will relax to this probability distribution in the long-time limit.

Eq. (3.2) expresses how transition matrix elements and the system energy profile depend on the sinusoidal function of the external perturbation. Here, the total energy $E_{\mathrm{i}}(k,\theta_0)$ of state i is a sum of the unperturbed state energy E_{i} and the perturbation contribution $-k\cos(\theta_{\mathrm{i}} - \theta_0)$.

θ_{i} is the angle of state i and θ_0 the angular orientation of the magnetic trap. The total energy $E^{\ddagger}_{\mathrm{i,i+1}}(k,\theta_0)$ of the barrier between adjacent states i and $i+1$ is the sum of the unperturbed barrier energy $E^{\ddagger}_{\mathrm{i,i+1}}$ and the perturbation contribution $-k\cos(\theta_{\mathrm{i,i+1}} - \theta_0)$,

where $\theta_{\mathrm{i,i+1}}$ is the angle of the energy barrier between states i and $i+1$. Transitions are only possible between adjacent states.

States A, C, and E are identical except for their different angle, such that a rotation of $\frac{2\pi}{3}$ radians would match them together (and likewise with the states B, D and F). So it is only the magnetic trap that breaks the symmetry.

We assume a chemical bath of ATP and ADP much larger than our system, such that the respective chemical potentials of ATP and ADP (and hence the chemical potential change upon chemical reaction) remain constant over the motor's operation. We model this by a constant energy difference ΔE_{chem} between each pair of mechanically identical but chemically distinct states (A and B, etc.).

In summary, the energy landscape of our thermodynamic system in the unperturbed regime can be described as

$$\begin{aligned} E_{\mathrm{A}} &= E_{\mathrm{C}} - \Delta E_{\mathrm{chem}} = E_{\mathrm{E}} - 2\Delta E_{\mathrm{chem}} \\ E_{\mathrm{B}} &= E_{\mathrm{D}} - \Delta E_{\mathrm{chem}} = E_{\mathrm{F}} - 2\Delta E_{\mathrm{chem}} \\ E_{\mathrm{B}} - E_{\mathrm{A}} &= E_{\mathrm{D}} - E_{\mathrm{C}} = E_{\mathrm{F}} - E_{\mathrm{E}} = \Delta E_{\mathrm{chem}}. \end{aligned} \tag{3.3}$$

As a result of having a free energy difference between the mechanically identical states (i.e. between $A-B$, $C-D$, and $E-F$), the energy landscape is effectively tilted. This tilt produces a spontaneous net rotation of the motor (in the absence of other driving forces).

Choosing the unperturbed energy of state A as our zero of energy, then combining Eq. (3.2) and Eq. (3.3) gives the total energy of each state as

$$\begin{aligned} E_{\mathrm{A}}(k,\theta_0) &= -k\cos(0-\theta_0) \\ E_{\mathrm{B}}(k,\theta_0) &= \Delta E_{\mathrm{chem}} - k\cos(0-\theta_0) \\ E_{\mathrm{C}}(k,\theta_0) &= \Delta E_{\mathrm{chem}} - k\cos\left(\frac{2\pi}{3}-\theta_0\right) \\ E_{\mathrm{D}}(k,\theta_0) &= 2\Delta E_{\mathrm{chem}} - k\cos\left(\frac{2\pi}{3}-\theta_0\right) \\ E_{\mathrm{E}}(k,\theta_0) &= 2\Delta E_{\mathrm{chem}} - k\cos\left(\frac{4\pi}{3}-\theta_0\right) \\ E_{\mathrm{F}}(k,\theta_0) &= 3\Delta E_{\mathrm{chem}} - k\cos\left(\frac{4\pi}{3}-\theta_0\right) \ . \end{aligned} \tag{3.4}$$

In order to simplify this model system, and hence the exploration of its parameter space, we further enforce additional symmetries. For simplicity, we put mechanical energy barriers exactly halfway between their corresponding metastable states. This means that we have mechanical energy barriers at $\frac{\pi}{3}$, $\frac{3\pi}{3}$, and $\frac{5\pi}{3}$, while chemical energy barriers have

the same angle as their corresponding metastable states. We also model ADP and ATP molecules as differing only by a chemical rearrangement; a more realistic picture would account for phosphate as a separate reactant. leading to transition rates dependent on phosphate concentration.

In addition, we also assume that the mechanical ($\Delta E^{\ddagger}_{\text{mech}}$) and chemical reaction barriers ($\Delta E^{\ddagger}_{\text{chem}}$) all have the same energy, before external perturbation by the rotary magnetic trap. Thus, the barrier energies including external perturbation are:

$$
\begin{aligned}
E^{\ddagger}_{\text{A,B}}(k,\theta_0) &= \Delta E^{\ddagger}_{\text{chem}} - k\cos(0-\theta_0) \\
E^{\ddagger}_{\text{B,C}}(k,\theta_0) &= \Delta E_{\text{chem}} + \Delta E^{\ddagger}_{\text{mech}} - k\cos\left(\frac{\pi}{3}-\theta_0\right) \\
E^{\ddagger}_{\text{C,D}}(k,\theta_0) &= \Delta E_{\text{chem}} + \Delta E^{\ddagger}_{\text{chem}} - k\cos\left(\frac{2\pi}{3}-\theta_0\right) \\
E^{\ddagger}_{\text{D,E}}(k,\theta_0) &= 2\Delta E_{\text{chem}} + \Delta E^{\ddagger}_{\text{mech}} - k\cos\left(\frac{3\pi}{3}-\theta_0\right) \\
E^{\ddagger}_{\text{E,F}}(k,\theta_0) &= 2\Delta E_{\text{chem}} + \Delta E^{\ddagger}_{\text{chem}} - k\cos\left(\frac{4\pi}{3}-\theta_0\right) \\
E^{\ddagger}_{\text{F,A}}(k,\theta_0) &= 3\Delta E_{\text{chem}} + \Delta E^{\ddagger}_{\text{mech}} - k\cos\left(\frac{5\pi}{3}-\theta_0\right) \\
E^{\ddagger}_{\text{A,F}}(k,\theta_0) &= E^{\ddagger}_{\text{E,F}}(k,\theta_0) - 3\Delta E_{\text{chem}} \ .
\end{aligned}
\tag{3.5}
$$

Considering the energies of all the states and barriers, the schematic representation of the unperturbed energy landscape is shown in Fig. 3.2.

The periodic nature of the external perturbation (a sinusoidal function) means that energy decreases in the vicinity of the trap center (external potential minimum), while energies of more distant states and barriers (those further away than $\pm\pi/2$ from the trap's center θ_0) are increased.

In summary, the energy landscape can in general be varied according to the finite-time driving protocol. In our simple model, k is the strength of the external perturbation, and θ_0 is the focus or minimum of the external potential. As control parameters vary in time, the system diffuses on the energy landscape and in general dissipates some quantity of heat, and also some quantity of work is spent on the system by the external manipulation of the control parameters.

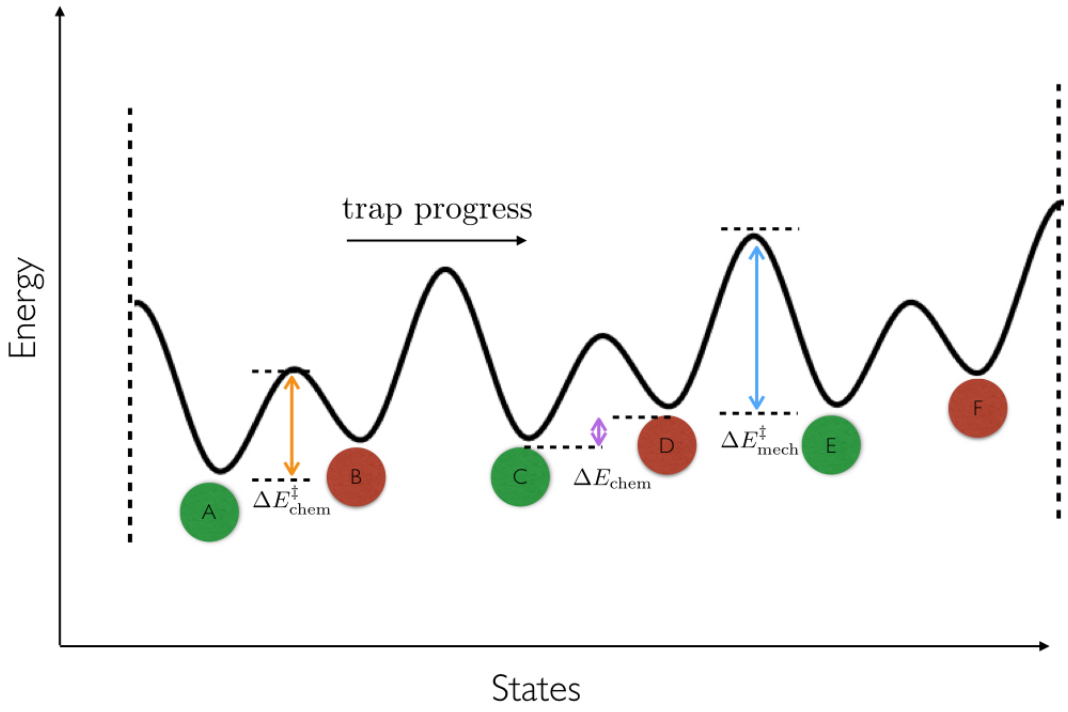

Figure 3.2: Schematic representation of the system's unperturbed energy landscape. One sequence of available states is represented alphabetically from A to F. Chemical reaction barriers of height $\Delta E^{\ddagger}_{\text{chem}}$ separate states $A-B$, $C-D$, and $E-F$, and are located at zero, $\frac{2\pi}{3}$, and $\frac{4\pi}{3}$, respectively. Mechanical barriers of height $\Delta E^{\ddagger}_{\text{mech}}$ separate states $B-C$, $D-E$, and $F-A$, and are located at $\frac{\pi}{3}$, $\frac{3\pi}{3}$, and $\frac{5\pi}{3}$, respectively. There is an energy offset $3\Delta E_{\text{chem}}$ between two adjacent series of six states due to the tight coupling between chemistry and mechanics (three ATP-ADP conversions regularly happen in each cycle of the motor's operation).

3.3 Work, heat, and ATP production

Experimentalists can externally manipulate F_1 via a time-dependent magnetic field acting on a magnetic bead attached tightly to the central crankshaft. Therefore, one can either do work on the system by rotating the magnetic field, or get work from ATP-ADP conversion occurring in the energetically favorable direction (reverse of the driving in our model).

Changing the control parameters changes the energy landscape of the system (see Eq. 3.4) and drives the system out of equilibrium. In our numerical calculations we quantify the accumulation of excess work, on average, at the following rate due to the variation in

the system's external control parameter θ_0:

$$\begin{aligned}\frac{\mathrm{d}W}{\mathrm{d}t} &= \frac{\mathrm{d}\theta_0}{\mathrm{d}t}\frac{\mathrm{d}U}{\mathrm{d}\theta_0} \\ \frac{\mathrm{d}U}{\mathrm{d}\theta_0} &= -k \sum_{\mathrm{i\ =\ A\ to\ F}} p_i \sin\left(\theta_i - \theta_0\right) \ .\end{aligned} \tag{3.6}$$

Dissipation of energy as heat transfer between the system and environment stems from probability flow between system states. We adopt the convention of heat flow into the system as positive. On average, heat transport across the system's boundaries occurs at the following rate

$$\begin{aligned}\frac{\mathrm{d}Q}{\mathrm{dt}} &= \left(p_{\mathrm{A}}T_{\mathrm{A,F}} - p_{\mathrm{F}}T_{\mathrm{F,A}}\right)\left(E_{\mathrm{F}} - E_{\mathrm{A}}\right) \\ &\quad + \left(p_{\mathrm{B}}T_{\mathrm{B,C}} - p_{\mathrm{C}}T_{\mathrm{C,B}}\right)\left(E_{\mathrm{C}} - E_{\mathrm{B}}\right) + \\ &\quad + \left(p_{\mathrm{D}}T_{\mathrm{D,E}} - p_{\mathrm{E}}T_{\mathrm{E,D}}\right)\left(E_{\mathrm{D}} - E_{\mathrm{E}}\right) \ .\end{aligned} \tag{3.7}$$

Finally, ATP production is quantified by the probability flow across chemical reaction barriers:

$$\frac{\mathrm{d[ATP]}}{\mathrm{d}t} = p_{\mathrm{A}}T_{\mathrm{A,B}} - p_{\mathrm{B}}T_{\mathrm{B,A}} + p_{\mathrm{C}}T_{\mathrm{C,D}} - p_{\mathrm{D}}T_{\mathrm{D,C}} + p_{\mathrm{E}}T_{\mathrm{E,F}} - p_{\mathrm{F}}T_{\mathrm{F,A}} \ . \tag{3.8}$$

A system's full cycle, 2π rotation of the central crankshaft, includes three jumps over the chemical reaction barriers and synthesis of three ATP from ADP, or in the reverse direction three ATP hydrolyzed into ADP.

In summary, this periodic rotary thermodynamic model system provides an approximate framework for calculating the nonequilibrium behavior of the F_1 ATP synthase motor protein.

Important system parameters include magnetic field orientation θ_0, magnetic field strength k, free energy difference ΔE_{chem} between reactant and products, height $\Delta E^{\ddagger}_{\mathrm{mech}}$ of mechanical energy barriers, and finally height $\Delta E^{\ddagger}_{\mathrm{chem}}$ of chemical reaction barriers. In other words, after taking into account reasonable simplifications motivated by the F_1 basic function and structure, we are now left with a much more manageable parameter space, easing the exploration of optimal driving protocols across this parameter space.

3.4 Model Simulation

In general, a stochastic process consists of a series of random events (jumps) such that each process (trajectory) can be described by a particular random walk across the state space. In this research project, we focus on investigating the ensemble average behavior of a rotary mechanochemical system as it is exposed to an external mechanical perturbation according

to a deterministic time schedule (a driving protocol). We investigate different protocols that each specify a time schedule for rotating the magnetic trap, changing θ_0, maintaining constant trap strength throughout. For this purpose, we focus on two fundamental quantities of our model system: the time-dependent probability distribution of occupying different states, and the probability current across the energy landscape. The probability distribution at equilibrium reflects how energetically favorable is a system state, while probability current across the energy landscape characterizes the average directed diffusive motion of the system as the external driving protocol proceeds, from an initial value to a designated final value on the control parameter space.

We hold the system in contact with a constant-temperature thermal bath. As described before, a thermodynamic system state is describable by two sets of separate variables. One set $\vec{x}(t)$ describes the internal state of the system at time t, and the other set $\lambda(t)$ describes the state of the external control parameters. $U(\vec{x}(t), \lambda(t))$ is the internal energy of the system at time t as a function of both the internal variables and external control parameters.

We divide the system's driving protocol into n successive steps, each of identical length equal to the relatively small time step Δt. Although we have considered a discretized time sequence, we choose a time step sufficiently small, around 1/1000 s, that discretization effects are negligible.

Evolution of the system is simulated over a given finite time interval, as the external control parameter is dynamically varied through a designated sequence of values $\{\lambda_0, \lambda_1, \ldots, \lambda_{\mathrm{n}}\}$ in control parameter space. One can designate a particular path through the control parameter space as

$$\vec{p}_0 \xrightarrow{\lambda_1} \vec{p}_1 \xrightarrow{\lambda_2} \vec{p}_2 \ldots \xrightarrow{\lambda_{\mathrm{n}}} \vec{p}_{\mathrm{n}} \ , \tag{3.9}$$

where at time $t = 0$, the system is in equilibrium with the thermal bath, its probability distribution is $\vec{p}_0$, and the external control parameter is λ_0. As the protocol proceeds, the nonequilibrium probability distribution is evolved by applying the transition matrix to the probability vector according to the master equation (Eq. (3.1)).

In general, each step consists of two substeps. First, the external control parameter changes from λ_i to the next point λ_{i+1}. This process is either resisted or assisted by the internal forces of the system that are exerted against/in favor of reconfiguration of the external agent. This external rearrangement, in general, performs work $U(\vec{p}_i(\vec{x}), \lambda_{i+1}) - U(\vec{p}_i(\vec{x}), \lambda_i)$ on the system.

Secondly, the system relaxes at fixed control parameter value λ_{i+1}, updating its probability distribution to $\vec{p}_{i+1}$. In this substep, heat $U(\vec{p}_{i+1}(\vec{x}), \lambda_{i+1}) - U(\vec{p}_i(\vec{x}), \lambda_{i+1})$ is transferred to the system. We repeat this one-timestep evolution until we reach the final designated control parameter value. Only the initial system distribution obeys the equilibrium Gibbs-

Boltzmann distribution, while at successive points $\vec{p}_1, \ldots, \vec{p}_n$, probability distributions are generally out-of-equilibrium because of the external driving forces.

Total work and total heat are a sum over all the heat and work collected during the individual steps

$$W = \sum_{i=0}^{n-1} U(p_i(\vec{x}), \lambda_{i+1}) - U(p_i(\vec{x}), \lambda_i) \tag{3.10}$$

$$Q = \sum_{i=1}^{n} U(p_i(\vec{x}), \lambda_i) - U(p_{i-1}(\vec{x}), \lambda_i) \ . \tag{3.11}$$

In accordance with the first law of thermodynamics, the average change in the system's internal energy equals the net energy added as heat to the system and the work done on the system by the external agent:

$$\Delta U_{\text{total}} = W + Q \ . \tag{3.12}$$

The average excess work that is required to be provided for the system to proceed in the control parameter space, in a finite time interval, is

$$W_{\text{ex}} = W - \Delta F \ , \tag{3.13}$$

where ΔF is the free energy difference of the system when the trap is at the final and at the initial states of the control parameter. Excess work is zero when the protocol is infinitely slow: when the required work equals the free energy difference.

3.5 Optimal protocols

In chapter 2 we saw that the optimal driving velocity is proportional to the inverse square root of the generalized friction coefficient $\zeta(\lambda(t))$:

$$\dot{\lambda}_{\text{opt}}(t) \propto \zeta(\lambda(t))^{-(1/2)} \ . \tag{3.14}$$

This generalized friction coefficient is the time integral of the force-force autocorrelation function, from $t = 0$ to $t = \infty$:

$$\zeta(\lambda(t_0)) = \beta \int_0^\infty \mathrm{d}t' \langle \delta X(0) \delta X(t') \rangle_{\lambda(t_0)} \ , \tag{3.15}$$

where δX is the deviation of the conjugate force from its equilibrium, ensemble average, value.

Our simplified thermodynamic model system has six available states and only one active control parameter θ_0, so the generalized friction coefficient is

$$\zeta(\lambda(t_0)) = \beta \sum_{n=0}^{\infty} \sum_{i,j=1}^{6} p^i_{\rm eq} \, [T^n]_{i,j} \, \Delta t \, \delta X_j \, \delta X_i \, , \tag{3.16}$$

where $p^{\rm i}_{\rm eq}$, $T_{i,j}$, and δX_i are the equilibrium probability of state i, transition rate from state i to state j, and deviation of the conjugate force associated with the state i from the equilibrium ensemble average force, respectively. The discrete-time dynamics is implemented through the transition rate matrix such that $T_{ij}\Delta t$ denotes the probability flux per time-step.

The first sum over timesteps n is the discretized equivalent of the time integral expression in Eq. (3.15), and the second sum over i, j averages the force autocorrelation function over the equilibrium distribution, for given control parameter value $\lambda(t_0)$. More specifically, $p^i_{\rm eq}[T^n]_{i,j}$ represents the probability of starting from the thermodynamic state i and ending up at the thermodynamic state j after n time-steps, at a fixed control parameter. According to the dynamics of our model system (represented by the 6x6 transition matrix), the system nonequilibrium distribution (and force-force correlation function) decays as a sum of five decaying exponential functions with different relaxation times. In the long-time limit, the correlation function can be approximated by a single decaying exponential function representing the slowest relaxing mode.

Due to the complexity of the system, we do not have an exact analytic expression of the force-force autocorrelation function. Practically, we approximate this time integral up to a specific time where the correlation has died down to less than 1/1000 of its initial value. We found that calculating to longer times has a negligible effect on our results. In other words, we cut the integral off beyond a certain time, and ignore the contribution of the rest of the time integral due to the insignificant value of the correlation in this long-time limit, where the system has basically forgotten its history.

Chapter 4

Results

In this chapter, the results and interpretation of our simulations are presented and discussed. Multiple computer simulations were done and subsequently analyzed to address the central questions posed in the introduction section of this thesis regarding the energetically optimal operation of the F_1 ATP synthase. The fundamental goal which guided our simulations and subsequent analysis was to find the optimized finite-time schedule (that which requires the smallest energy input from external energy resources) of mechanically perturbing a rotary mechanochemical molecular-scale motor around its operational cycle.

Our initial simulations primarily characterized the generalized friction coefficient in the model of F_1-ATPase performance in response to external mechanical perturbation. In this respect, we have explored different regions of parameter space to evaluate this quantity under different conditions in order to be able to describe the optimal driving protocols both qualitatively and quantitatively. Additionally, we compared simulation-based exact observable expectations with the approximate near-equilibrium theoretical expectations involving the friction coefficient to assess the validity of our description of optimal protocols in the limit of finite-time, but slow, driving operations.

We explore our model system by characterizing a parameter regime corresponding approximately to practical, slow-varying, magnetic tweezers experiments on single F_1-ATPase [28], where the rotational diffusion coefficient is assumed to be dominated by the contribution from a micron-sized magnetic bead, approximated as a sphere of radius $r = 10^{-6}$m with a hydrodynamic rotational diffusion coefficient [68]

$$D = \frac{k_{\mathrm{B}}T}{8\pi\eta r^3} \ . \tag{4.1}$$

The micron-sized magnetic bead thus has $D_{\mathrm{bead}} = 0.25\ \mathrm{rad}^2/\mathrm{s}$. Here, $\eta = 7{\times}10^{-4}\ \mathrm{kg/m.s}$ is the viscosity of water at typical body temperature, $T = 310$ K. The hydrodynamic diffusion coefficient of the isolated F_1's central shaft has been estimated to be around

$D_{\text{shaft}} = 0.07$ rad^2/ns [37], thus in this setup rotational diffusion of the magnetic bead is dominant due to the considerably larger physical dimensions.

Our transition rates in Eq. 3.2 do not have an inherent time unit. Given the transition rates, we calculate the system's mean square angular displacement and ultimately the diffusion coefficient of the system in a flat energy landscape. Then by equating our diffusion coefficient with the approximate diffusion coefficient in Eq. 4.1, we grant a proper physical meaning to the time unit of our simulation and hence the system transition rates.

4.1 Generalized friction coefficient

Intuitively, the generalized friction coefficient quantifies the resistance of a physical system against external perturbations, and could characterize system dissipation as well as the optimal driving protocols in the near-equilibrium regime. The friction coefficient is the time integral of the conjugate force autocorrelation function, which can be decomposed into the product of the conjugate force variance (the zero-time autocorrelation) and the integral relaxation time [Eq. (2.16)]. Based on the energy landscape (Fig. 3.2) defined for our thermodynamic system in the previous chapter, we calculate this quantity for different values of our model parameters (Fig. 4.1). For example, we vary perturbation (magnetic trap) strength, mechanical barrier height, and chemical reaction barrier height.

The structural threefold symmetry of the F_1 ATPase (discussed in the Introduction) enters our model as a sequence of periodic states on a ring. This leads to a friction coefficient $\zeta(\theta_0)$ that is a periodic function of magnetic field angular position θ_0, with a periodicity of $\frac{2\pi}{3}$ matching the system's internal periodicity. For simplicity, we have only reported the friction in the first period of our system, namely from 0^o to 120^o, since other periodic images will give identical results.

As demonstrated in Fig. 4.1, the generalized friction coefficient varies significantly upon varying internal and external parameters such as trap strength k, mechanical and chemical reaction barrier heights ($\Delta E^{\ddagger}_{\text{mech}}$ and $\Delta E^{\ddagger}_{\text{chem}}$) and trap minimum θ_0. Numerical simulations, as intuitively anticipated, show minima and maxima in resistance around the metastable states and mechanical energy barriers, respectively. Intuitively, the system rapidly relaxes within a metastable state, so the generalized friction coefficient should be relatively small when the trap's minimum is near a metastable state.

On the other hand, when the trap minimum is near a mechanical barrier, the corresponding equilibrium distribution has significant probability on either side of the energy barrier, and consequently the conjugate force correlation time is maximized, leading the system to have peaks in its resistance against external manipulations around the three mechanical barriers. In the specific range that we have explored, in particular when a strong magnetic field is applied, the generalized friction coefficient varies significantly, by more than eight orders of magnitude, indicating that dissipation could be notably different when the driving

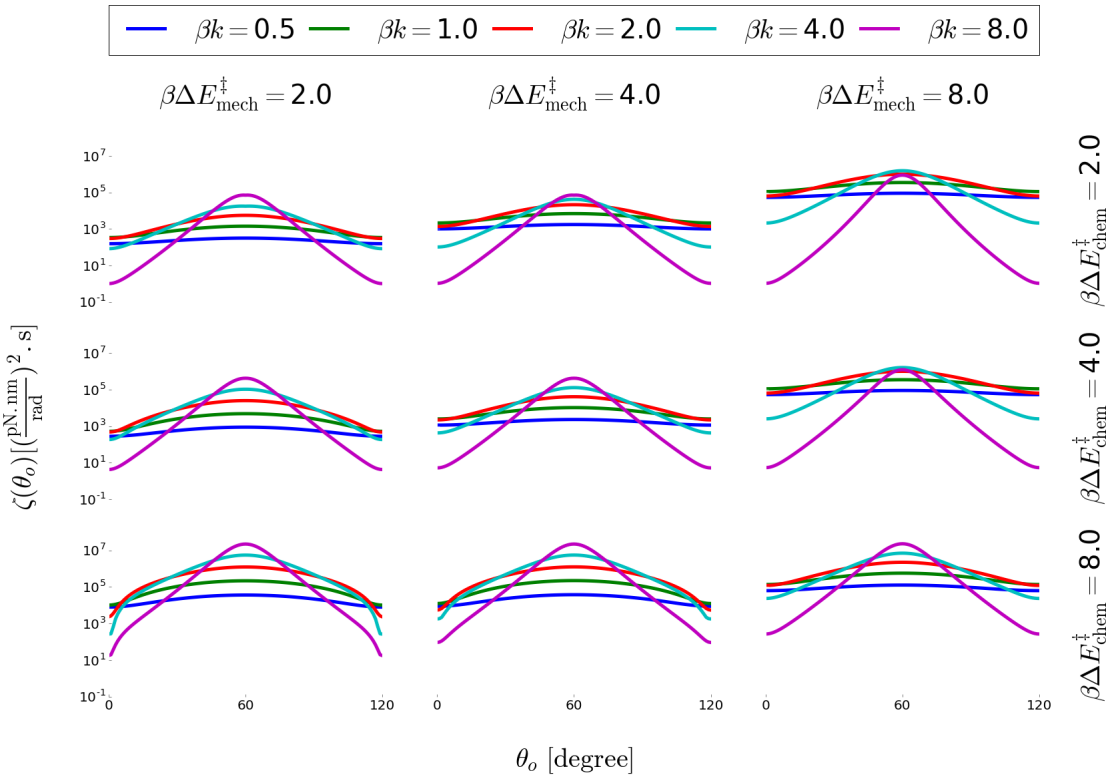

Figure 4.1: The generalized friction coefficient, across a range of trap minima θ_0, for varying mechanical and chemical reaction barrier heights $\Delta E^{\ddagger}_{\mathrm{mech}}$ and $\Delta E^{\ddagger}_{\mathrm{chem}}$, left to right and top to bottom, respectively, while $\Delta E_{\mathrm{chem}} = 0$. Different colors within a given sub-plot show different trap strengths.

protocol proceeds near the potential well rather than in the vicinity of mechanical barriers. What we actually observe here is that when there are low barrier heights and weak perturbing traps, the friction coefficient is relatively flat and small, not varying with the trap's time-dependent minimum. As trap strength increases, the friction coefficient varies more and more across the control parameter space. This implies that the system requires a non-uniform control protocol velocity to minimize the required work.

For the system to proceed alongside the driving protocol (in phase), it must overcome the activation energy barriers. The larger the energy barriers $\Delta E^{\ddagger}_{\mathrm{chem}}$ and $\Delta E^{\ddagger}_{\mathrm{mech}}$, the larger the difference between the transient states and the initial metastable states, the harder it is for the process to actually happen. This is due to smaller transition rates leading to longer relaxation times which, in turn, leads to a larger friction coefficient. In other words, for a process or a chemical reaction to proceed in a preferred direction, the thermodynamics must be energetically favorable (i.e. the energy difference between initial and final metastable states must be considerable), and the kinetics must be reasonably rapid (i.e. transition rates must be large). The magnetic trap perturbs the energy landscape such that it makes states located around its center (minimum energy) energetically favorable,

and it also lowers the energy barriers in close neighborhood of its center, and hence the system would be stimulated to flow towards the center of the magnetic trap. Therefore, the stronger the magnetic trap k the easier it is for the system to follow the magnetic trap.

4.2 Optimal driving velocity

According to the theoretical framework that we have discussed in the theory chapter, the optimal driving protocol keeps excess power constant over the entire time interval of the control protocol, which proceeds in a way that the velocity of the changing control parameter is proportional to the inverse square root of the generalized friction coefficient at the corresponding point of control parameter space [17]:

$$\left(\frac{\mathrm{d}\theta_0}{\mathrm{d}t}\right)_{\mathrm{opt}} \propto \zeta(\theta_0)^{-1/2} \ . \tag{4.2}$$

This relation clearly does not depend on the time length of the driving protocol but is expected to characterize optimal protocols more accurately in the limit of long time intervals when the system is closer to the equilibrium distribution. Given the variation in the generalized friction coefficient (Fig. 4.1), the optimal control parameter velocity (Fig. 4.2) varies by orders of magnitude across a given driving protocol, leading to an optimal protocol that is significantly distinguishable from the naive (constant-velocity) protocol (Fig. 4.3). In the specific range we explored, in the case of very strong magnetic fields, optimal velocities vary more than three orders of magnitude.

As demonstrated in Fig. 4.2, as energy barriers go from low to high, the optimal driving velocity around the energy barriers goes from high to low, indicating that near high energy barriers, the system should be driven slow in order to keep the nonequilibrium probability distribution more similar to the equilibrium distribution. In other words, we need to give the system enough time to successfully jump over the energy barrier due to thermal fluctuations, so it can ultimately follow, in phase, the magnetic field's dynamic rotation.

4.3 Optimal driving protocol

The optimal protocol represents the time schedule by which one externally perturbs the system that minimizes the amount of energy that must be externally supplied. The key intuition from the optimal driving velocity patterns in Fig. 4.2 is that the optimal protocol proceeds relatively fast when the system can quickly relax, providing low friction or resistance, in order to leave extra time in regions where friction is large, thus giving thermal fluctuations extra time to kick the system over barriers without requiring work.

We observe that when the generalized friction coefficient is relatively flat, the system generally proceeds according to the naive protocol and so there is no significant energy saved

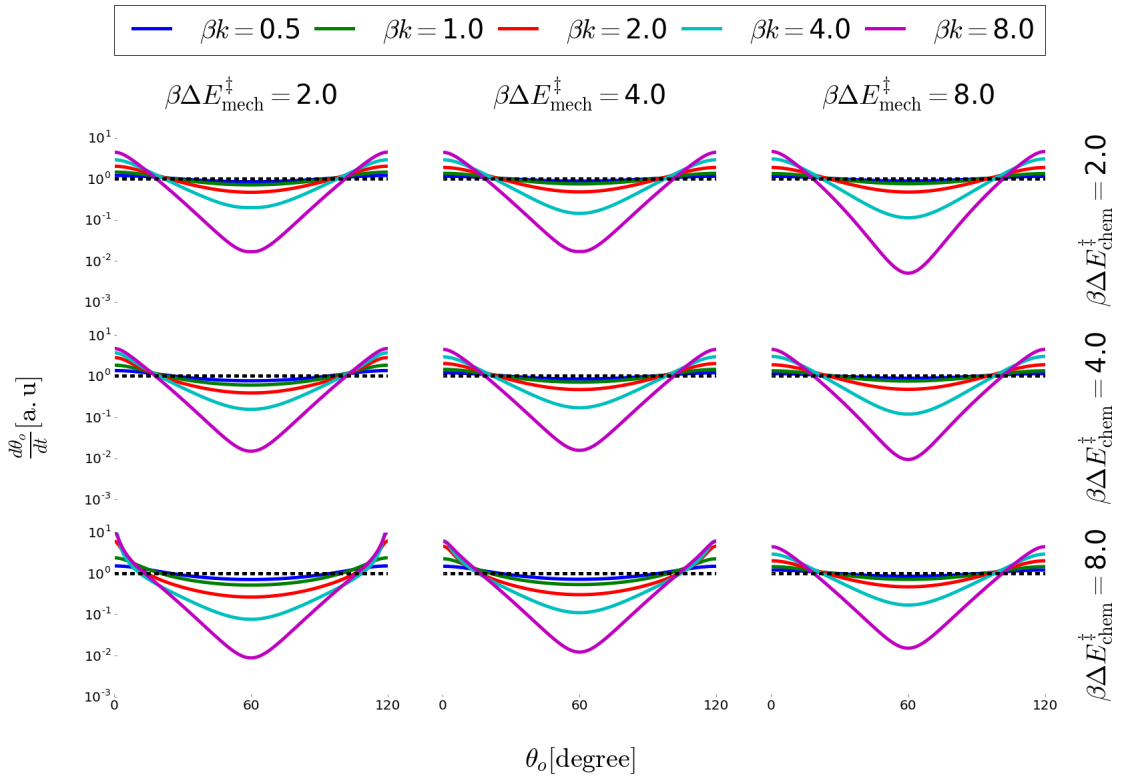

Figure 4.2: Optimal driving velocity $\frac{\mathrm{d}\theta_0}{\mathrm{d}t}$ of control parameter θ_0 (in arbitrary units) as a function of the control parameter, for naive constant-velocity protocols (dashed lines) and optimal driving protocols under the linear response approximation (solid curves). Same variation of k, $\Delta E^{\ddagger}_{\mathrm{mech}}$, and $\Delta E^{\ddagger}_{\mathrm{chem}}$ as in Fig. 4.1, with $\Delta E_{\mathrm{chem}} = 0$

by performing the optimal protocol, but when we have a non-uniform friction coefficient across the control parameter space, the deviations of the optimal protocol from the naive protocol are much larger and ultimately influential in the system's operation.

The optimal protocols provide a higher chance for the system to make effective use of the external free resource of energy, namely, thermal fluctuations from the surrounding thermal bath,. After a transition from one side of the barrier to the other side has been done at a slow speed, the optimal protocol again proceeds relatively quickly until nearing the next mechanical barrier.

4.4 Excess power

The total excess work of a given physical process proceeding between two particular points in control parameter space is important because it represents how efficiently a system (such as a motor) operates during a designated finite-time driving protocol. This quantity can be evaluated by a time integration over the excess power, which is naturally a time-dependent function throughout the entire driving time.

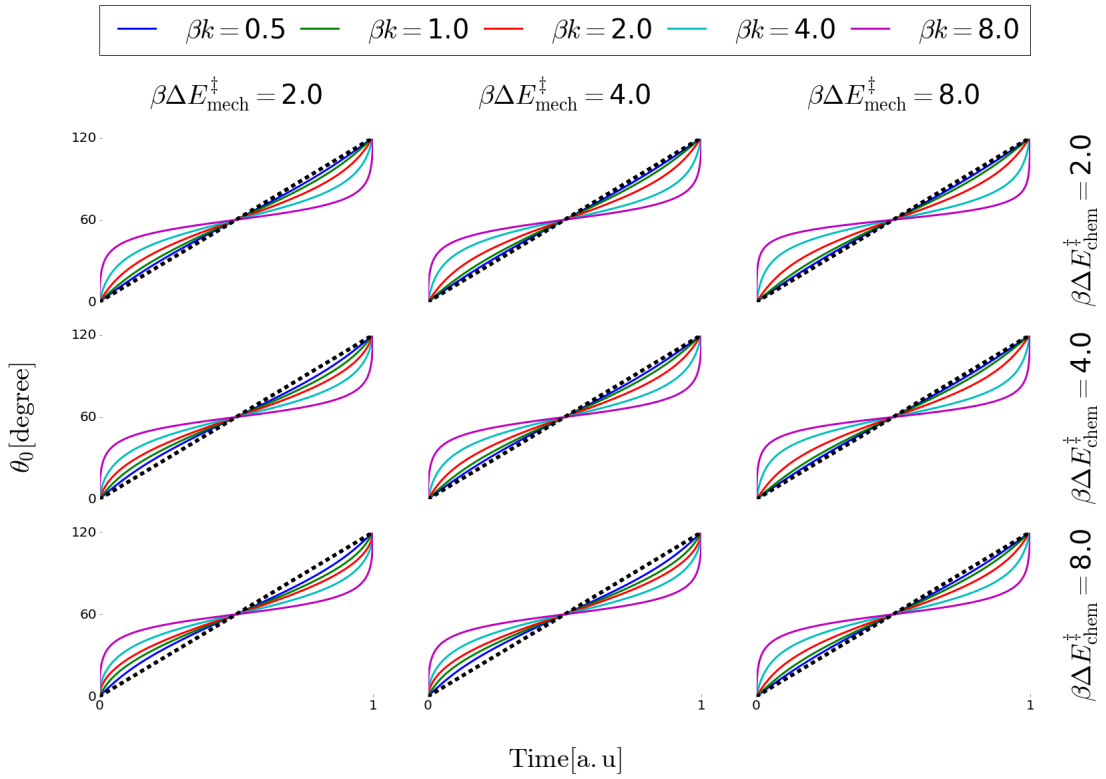

Figure 4.3: Optimal driving protocols. Control parameter position θ_0 as a function of time (in arbitrary units), for naive constant-velocity protocols (black dashed lines) and optimal protocols under the linear response approximation (solid curves). Same variation of k, $\Delta E^{\ddagger}_{\mathrm{mech}}$, and $\Delta E^{\ddagger}_{\mathrm{chem}}$ as in Fig. 4.1.

We estimate this excess power during naive (constant velocity) protocols using the outlined near-equilibrium approximation, Eq. (2.12). This specific equation, as well as the entire optimal driving protocol framework, is a linear response approximation, so it would be beneficial to check how well the approximation works across model parameters. In this regard, we directly calculate the exact excess power from numerical simulation of the system dynamics as discussed in "Model Simulation" (see Eq. (3.10)) to assess the validity of the approximate analytic theory in the investigated parameter ranges.

As can be seen in Fig. 4.4, in the regime of low energy barriers, the approximate description of excess power matches almost perfectly with the numerical exact calculation of excess power. This is because the system has settled down into a NESS that is not too far from equilibrium. However, for high energy barriers and weak traps, the approximation does not align perfectly with the numerical calculation. We observe breakdowns in a couple different ways, one of which is that the exact (numerical) work is below the theoretical prediction at very small times. This is because the system starts from an initial equilibrium distribution and has not yet reached its steady-state distribution. By contrast, the theory essentially assumes the system is always at a steady-state distribution at a particular distance from

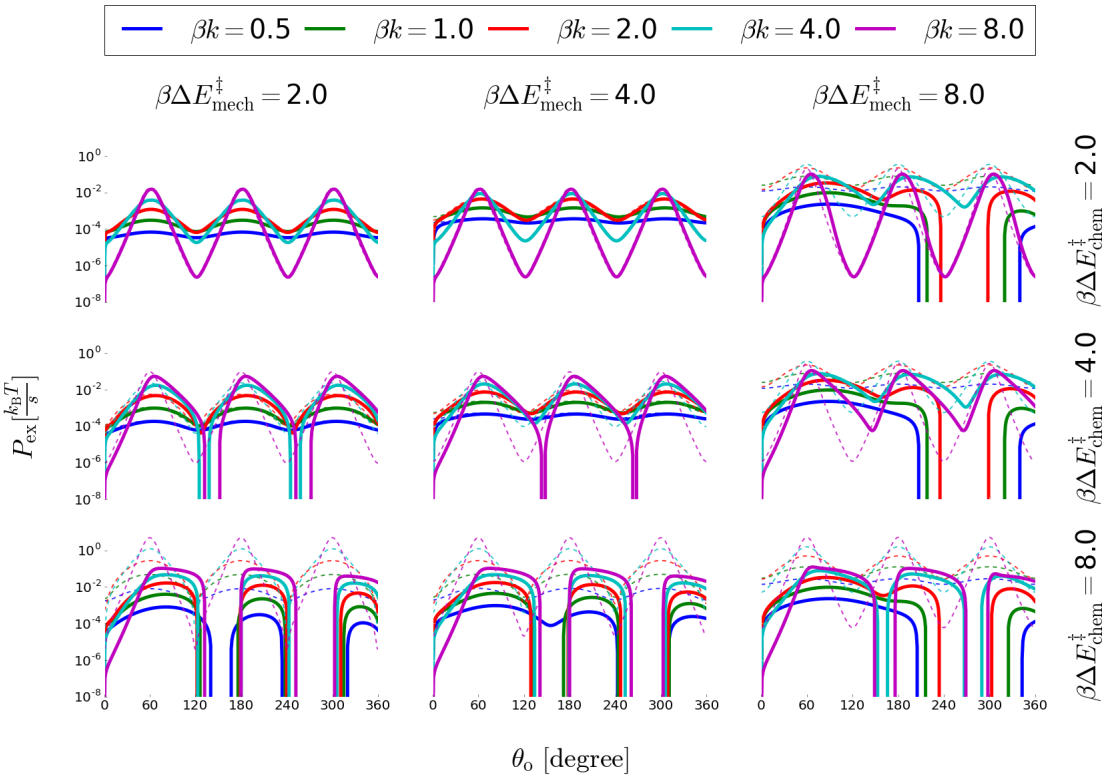

Figure 4.4: Excess power P_{ex} as a function of control parameter θ_0, calculated directly via numerical simulation (solid curves) or estimated using the control parameter velocity and the generalized friction coefficient (dashed curves). Magnetic field rotation angular velocity is $\sim 10^{-3}$ Hz. Same variation of k, $\Delta E^{\ddagger}_{\mathrm{mech}}$, and $\Delta E^{\ddagger}_{\mathrm{chem}}$ as in Fig. 4.1. For large energy barriers, around 150^o and 270^o the excess power becomes negative.

equilibrium. Another breakdown is that for large energy barriers and a weak magnetic trap, at later times the exact excess work exceeds the theoretical prediction. This occurs when the protocol proceeds sufficiently rapidly that the system gets stuck behind the energy barrier because it does not have enough time to transition to the other side of the energy barrier, so its distribution lags far behind (and hence is far from equilibrium). In general, the approximate description of excess power is valid when the system probability distribution is sufficiently close to the Gibbs-Boltzmann equilibrium probability distribution.

For really large energy barriers, the system's distribution get stuck on the wrong side of the energy barrier (see Fig. 4.7), while the the near-equilibrium approximation implicitly assumes that the system is only 'locally' out of equilibrium. Moreover, contrary to the case of transitions between equilibrium states where excess power is greater than or equal to zero, $P_{\mathrm{ex}}(t) \geq 0$, excess power can in general be less than zero due to the periodic nature of the perturbation. We note that the height of energy barriers in an ATP synthase molecule has been approximated [39] to be twice higher than the larger energy barrier that we have investigated here.

Thus for a system approximated by a near-equilibrium theoretical framework, remaining close-to-equilibrium distribution is an important criterion. As can be seen in Fig. 4.4, the approximate results do not agree with numerical calculations for large energy barriers. We quantify this difference from the equilibrium distribution by the relative entropy between nonequilibrium and equilibrium probability distributions

$$D(p(x)||q(x)) = \sum_{\mathrm{x}} p(x) \log \left[\frac{p(x)}{q(x)}\right] , \tag{4.3}$$

is a measure of the difference between two different probability distribution $p(x)$ and $q(x)$ [40]. Relative entropy is non-negative [40], equaling zero if and only if the two distributions match perfectly, $p(x) = q(x)$. Although, it is not a true distance metric between distributions since it is not symmetric (and doesn't satisfy the triangle inequality), it is useful to consider relative entropy as a measure of how distinct two distributions are. In this regard, we can compare the system's nonequilibrium probability distribution $p_i^{\mathrm{noneq}}(\theta_0)$ with the corresponding equilibrium probability distribution $p_i^{\mathrm{eq}}(\theta_0)$, to quantify how much the system distribution departs equilibrium. Moreover, the free energy difference between two different probability distributions, but with identical control parameter, one representing an equilibrium probability distribution and one representing an out-of-equilibrium probability distribution, is equal to the relative entropy between the two distributions [41, 42].

As demonstrated in Fig. 4.5, when the protocol (magnetic trap minimum) proceeds between $0^o \rightarrow 60^o$ degrees, $D(P^{\mathrm{noneq}}||P^{\mathrm{eq}}) \approx 0$, implying that the nonequilibrium and equilibrium probability distributions are almost equal. However, as the protocol proceeds further, the nonequilibrium distribution departs from the equilibrium one. Details of the departure essentially depend on the height of energy barriers, strength of the magnetic trap, and velocity of driving protocols. For large energy barriers, namely sub-plots to the right and bottom, the system evidently could not cross the energy barriers. However, in other cases, the system partially relaxes toward the current equilibrium distribution, leading to a reasonable approximation for the excess power represented in Fig. 4.4.

Furthermore, as demonstrated in Fig. 4.5, the system more rapidly crosses energy barriers when it's driven on an optimal protocol rather than a naive (constant-velocity) protocol. Near the energy barriers, the velocity of the optimal protocol is much lower than the velocity of the naive protocol (Fig. 4.2), and thus provides more time for the system to successfully cross over the energy barrier and relax toward the current equilibrium distribution.

There are many close-to-equilibrium theoretical frameworks whose physical description is valid when the system remains sufficiently close to equilibrium. Based on our calculation, optimal driving protocols provide an intuitive method to keep the system under investigation closer to equilibrium than what naive protocols do [67].

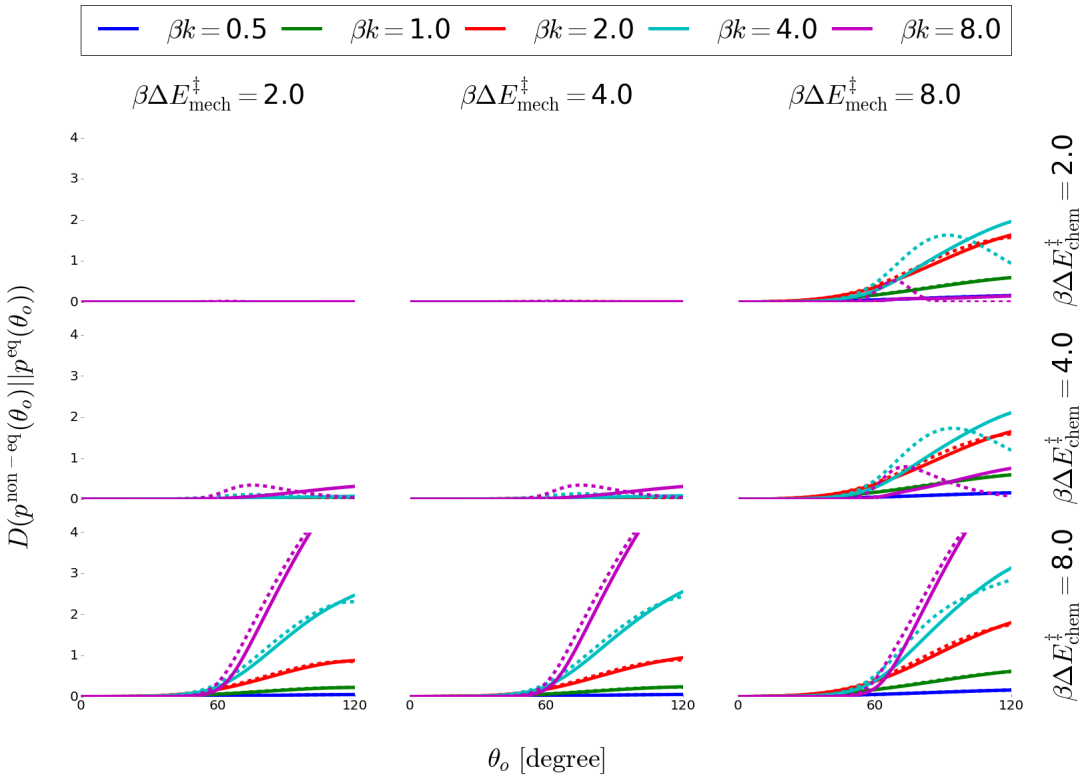

Figure 4.5: Relative entropy $D(p^{\mathrm{noneq}}||p^{\mathrm{eq}})$(numerical result), between nonequilibrium and equilibrium probability distributions as a function of control parameter θ_0, for naive (constant-velocity) protocols (solid curves) and optimal protocols under the linear response approximation (dashed curves). Magnetic field angular velocity is $\sim 10^{-3}$ Hz. Same variation of k, $\Delta E^{\ddagger}_{\mathrm{mech}}$, and $\Delta E^{\ddagger}_{\mathrm{chem}}$ as in Fig. 4.1.

4.5 Efficiency ratio

The ratio of $W_{\mathrm{ex}}^{\mathrm{naive}}$ (total excess work during a naive driving protocol) to $W_{\mathrm{ex}}^{\mathrm{optimal}}$ (total excess work during an optimal driving protocol) quantifies the enhancement in efficiency from driving this rotary mechanochemical stochastic motor on the optimal path rather than the naive, constant velocity, driving protocol. A straightforward derivation [22] (see Appendix A) shows that, in the regime of the linear-response approximation, this ratio depends simply on the generalized friction coefficient value across the protocol, equaling the ratio of the average friction coefficient to the square of the mean square-root friction coefficient:

$$\frac{W_{\mathrm{ex}}^{\mathrm{naive}}}{W_{\mathrm{ex}}^{\mathrm{optimal}}} = \frac{\overline{\zeta}}{\overline{\zeta^{1/2}}^{2}} \ . \tag{4.4}$$

The average is over all control parameter points across the driving process,

$$\overline{\zeta} \equiv \frac{\int_0^{2\pi} \zeta(\theta_0)\, \mathrm{d}\theta_0}{2\pi} \ . \tag{4.5}$$

Although this measure of friction coefficient variation is independent of the protocol time, its accuracy in approximating the actual excess work ratio depends on the protocol time, working best in the limit of relatively slow protocols, when the system stays sufficiently close to the equilibrium. In the range that we have explored our system, this ratio reaches as high as 4.0 (Fig. 4.6).

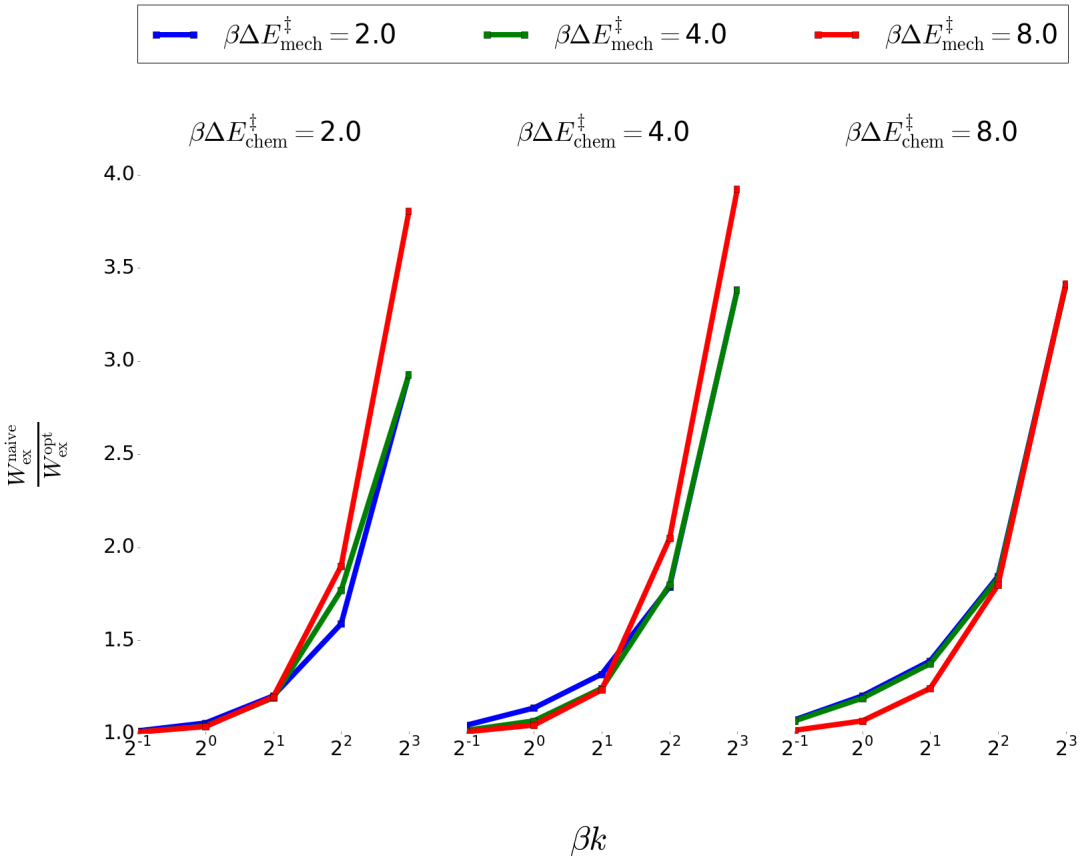

Figure 4.6: Ratio of total excess work during the naive protocol to total excess work during the optimal driving protocol, estimated from the linear-response approximation. Same variation of k, $\Delta E^{\ddagger}_{\mathrm{mech}}$, and $\Delta E^{\ddagger}_{\mathrm{chem}}$ as in Fig. 4.1.

The takeaway from Fig. 4.6 is that in the limit of very non-uniform friction coefficient (Fig. 4.1), when the system is exposed to a relatively strong external perturbation, there is a considerable benefit (in work saved) in performing an optimal protocol rather than a naive one. This difference may be interesting in investigation of biological systems or when one intends to design efficient stochastic nanometer-scale motors. Curves with different mechanical barriers can cross the trap strength k increases (middle subplot in the above

picture). In a similar study of optimal crossing of a single mechanical barrier, crossovers were not detected [22]. Though we have note identified the necessary and sufficient conditions, in our more complicated system, the periodic boundary conditions, multiple barriers/basins and coupling between mechanical motion and a chemical reaction all may contribute to this crossover.

4.6 Net rotation

As pointed out in the previous chapters, a full cycle of the system's operation (a full 360^o rotation of the central crankshaft) requires three ADP molecules to convert to three ATP molecules. Conversely, full rotation in the reverse direction converts three ATP molecules to three ADP molecules. In this respect, net rotation of the system per one cycle of magnetic field rotation, denoted by $\overline{n}$, is an important measure of useful output in our simulation. We calculate this through the nonequilibrium probability flow according to Eq. 3.8 and plot it in Fig. 4.7. $\overline{n}$ is unity when the system, on average, rotates 2π during a single 2π protocol.

Although for large mechanical energy barriers and weak magnetic fields (leftmost points in the red curves), the system is biased toward rotation along with the magnetic field, it does not completely follow the trap's time-dependent rotation. For low energy barriers or strong magnetic fields (right-most points in all curves), the system more easily follows the trap rotation.

In the regime that we have explored and for weak magnetic fields, optimal driving protocols are not significantly different from naive (constant-velocity) driving protocols (Fig. 4.3), and thus the system's net rotation is not a sensitive function of the driving protocols (Fig. 4.7). However, the system's net rotation during the optimal and naive protocols are distinguishable for strong magnetic fields.

For very large energy barriers, especially large chemical reaction barriers (right curves with $\Delta E^{\ddagger}_{\text{chem}} = 8\ k_{\text{B}}T$), the system gets stuck behind the barriers and can not rotate with the magnetic bead. The external perturbations affect transition rates representing mechanical rotation, but they do not facilitate or impede transition between chemical states (since the chemical reactions do not change the mechanical coordinate), so large chemical reaction barriers make it extremely difficult for the system to follow the trap's lead.

4.7 Tilted energy landscape

It has been recently shown that the optimal theoretical framework [17] is applicable for finding optimal protocols in slow transitions between nonequilibrium steady states (NESS) [12] that could be, in general, far from thermal equilibrium. In this generalization, elements of the friction tensor are given by the time integral of the conjugate force autocorrelation function averaged over the NESS probability distribution. In other words, this generalization

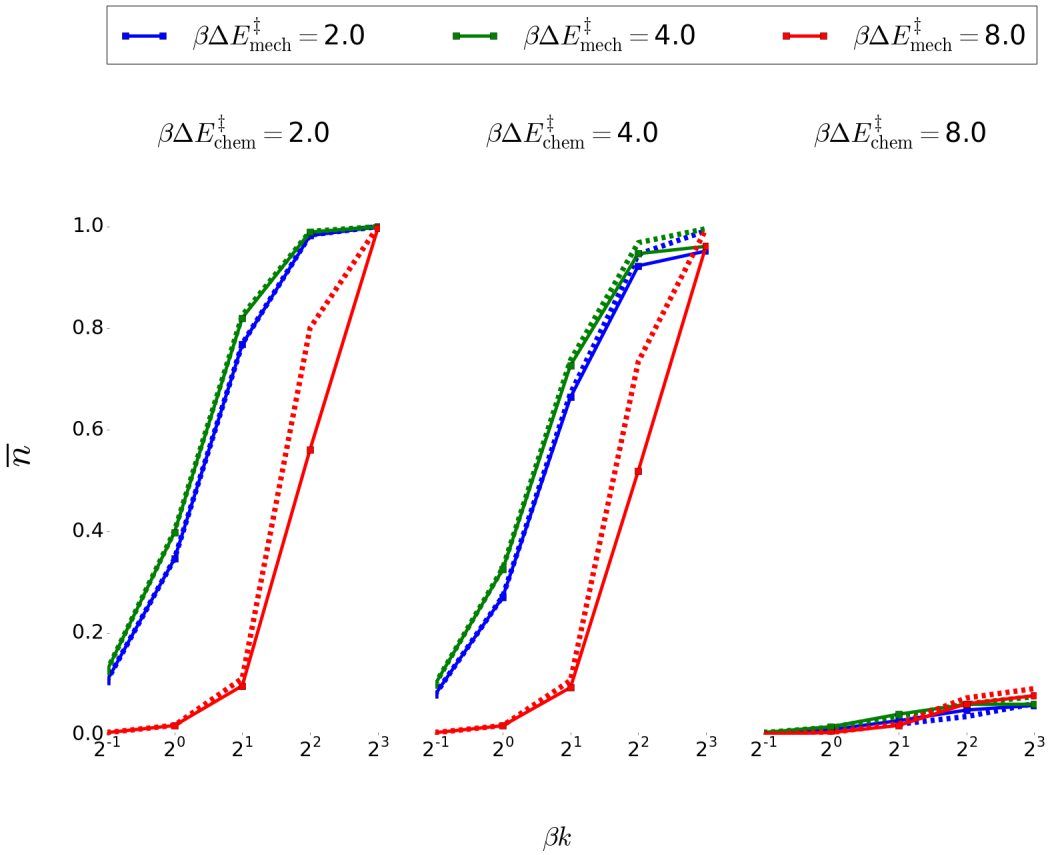

Figure 4.7: System net rotation per one cycle of optimal driving protocols (dashed curves) and naive (constant-velocity) driving protocols (solid curves). Same variation of k, $\Delta E^{\dagger}_{\mathrm{mech}}$, and $\Delta E^{\ddagger}_{\mathrm{chem}}$ as in Fig. 4.1.

establishes a connection between excess dissipation and stationary thermal fluctuations in the NESS, while, for near equilibrium transitions, the friction tensor is evaluated by the equilibrium thermal fluctuations (Fig. 4.8), and subsequently, the optimal driving velocity, and optimal protocol, has been calculated in Fig. 4.9 and Fig. 4.10, respectively.

ΔE_{chem} denotes how energetically favorable the reactant molecules are compared to the product molecules, which are ATP and ADP molecules here. In the previous sections of this chapter, we have assumed $\Delta E_{\mathrm{chem}} = 0$ in order to enforce that the system probability distribution is distributed according to the equilibrium Gibbs-Boltzmann distribution: six periodic states with equal bare energy levels (when the magnetic trap is off). This assumption is relaxed for this section and the system is free to have spontaneous transitions between nonequilibrium steady states. Although the Gibbs-Boltzmann equilibrium distribution does not depend on the height of energy barriers, the NESS distribution depends on the height of the energy barriers, and thus is characterized through the specification of energy barrier heights as well as all the state energy levels. A full cycle of the system's operation basically requires more than $3\Delta E_{\mathrm{chem}}$ units of energy to be spent on the system

to be able to convert three low-energy ADP molecules to three high-energy ATP molecules, and in the reverse direction, which is more energetically favorable, this energy would be released by the system as saved chemical energy.

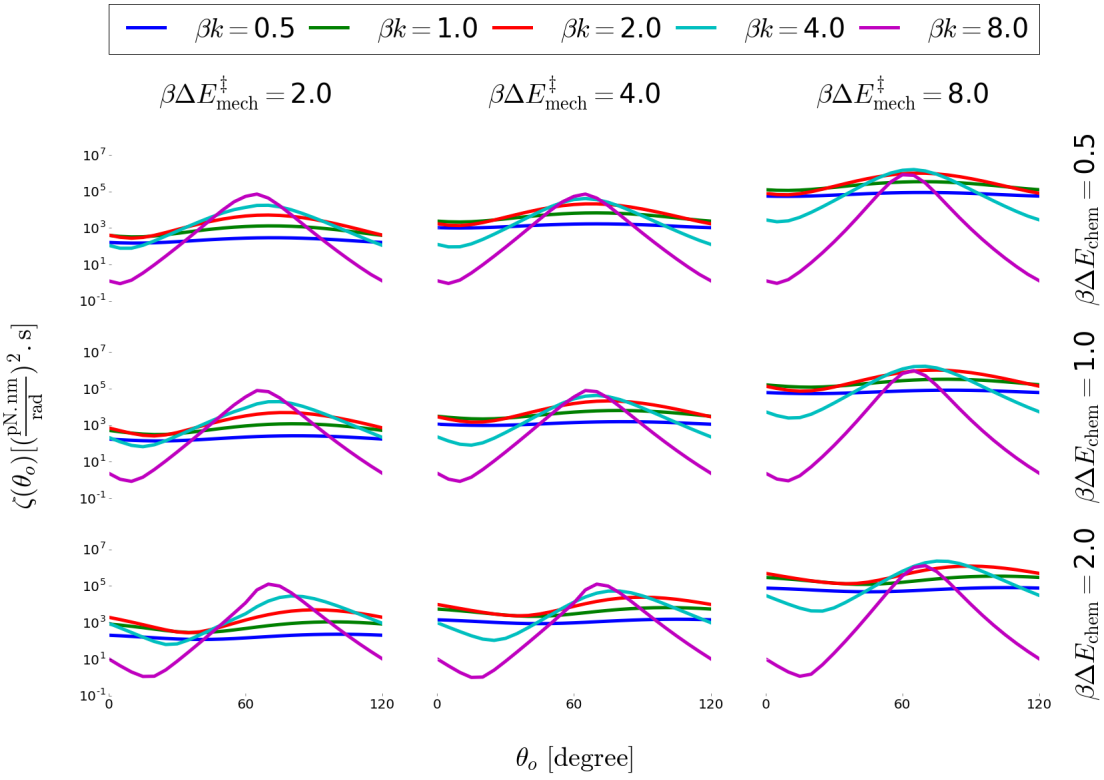

Figure 4.8: The generalized friction coefficient at the NESS, across a range of trap minima θ_0, for varying mechanical energy barriers heights, $\Delta E^{\ddagger}_{\mathrm{mech}}$ and chemical free energy differences, ΔE_{chem}, left to right and top to bottom, respectively. Trap magnitude is represented by different colors within a given sub-plot. Chemical energy barrier height $\Delta E^{\ddagger}_{\mathrm{chem}}$ is set to 2 $k_{\mathrm{B}}T$.

For a small chemical energy difference between metastable states (i.e. $\Delta E_{\mathrm{chem}} \ll 1$), the system responds as an equilibrium system such that maximum and minimum values of generalized friction coefficient are close to the location of mechanical energy barriers and metastable states, respectively. However, increasing ΔE_{chem} pushes the system distribution away from equilibrium and can be characterized by a markedly different NESS probability distribution, where friction coefficient peaks and troughs are not located exactly at the mechanical energy barriers and metastable states, in contrast with the equilibrium distribution. We show this shift in NESS distribution minima and maxima in Fig. 4.8.

The intuition here is that the generalized friction coefficient is maximal when two metastable states are equally probable, and hence equally energetically favorable. For instance, when $\Delta E_{\mathrm{chem}} = 0$, states are equally energetic favorable when the trap is exactly halfway between the two sites, so a trap located at 60^o makes $A - B$ and $C - D$ equally

energetically favorable. In contrast with the equilibrium description (when $\Delta E_{\text{chem}} = 0$), for $\Delta E_{\text{chem}} > 0$ states are equally energetically favorable when the trap is inclined towards the higher energy site (i.e. a rightward shift of the trap) rather than being exactly halfway between the metastable states. As intuitively expected, this shift is an increasing function of ΔE_{chem} (Fig. 4.8). Minima are also shifted to the right. Intuitively, the friction coefficient is minimized when the probability is overwhelmingly in a specific microstate. Due to the tilt in the energy landscape, the probability of a state is maximized when the trap minimum is to the right of the state rather than exactly at the state.

4.7.1 Optimal driving velocity

Taking into account the variation in the generalized friction coefficient shown in Fig. 4.8, the optimal driving velocity is shown in Fig. 4.9. It varies by orders of magnitude across a given finite-time protocol, leading to optimal protocols that are considerably different from naive (constant-velocity) driving protocols (Fig. 4.10). In the specific range that we have explored, in the case of very strong magnetic fields, optimal velocities vary over a single protocol by more than three orders of magnitude.

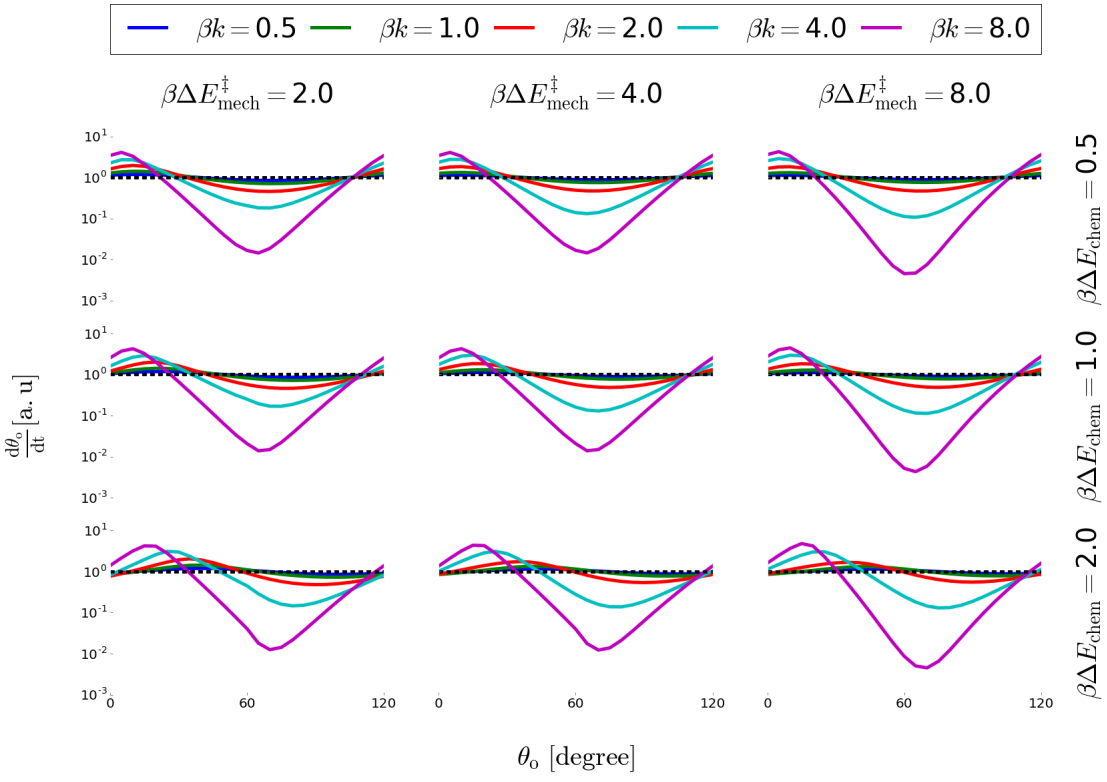

Figure 4.9: Optimal velocity $\frac{\mathrm{d}\theta_0}{\mathrm{d}t}$ (in arbitrary units) of control parameter θ_0 as a function of control parameter, for naive constant-velocity protocols (dashed lines) and optimal protocols under the linear-response approximation (solid curves). Chemical energy barrier height $\Delta E^{\ddagger}_{\text{chem}} = 2\ k_{\text{B}}T$. Same variation of k, $\Delta E^{\ddagger}_{\text{mech}}$, and ΔE_{chem} as in Fig. 4.8.

In correspondence with the shift in friction coefficient curves, optimal driving velocity minima and maxima are also shifted towards the higher energy states such that optimal driving velocity is relatively slow when two adjacent states are equally energetically favorable, giving the system more time to be kicked over the mechanical energy barrier by a thermal fluctuation. On the other hand, the protocol proceeds relatively quickly when the trap is near the minima of the NESS distribution, where the system rapidly relaxes to the nonequilibrium steady-state distribution.

4.7.2 Optimal driving protocol

Due to the friction tensor shifts (Fig. 4.8), the most significant difference in optimal driving between nonequilibrium steady states (Fig. 4.10) and equilibrium states (Fig. 4.3) is that in the latter case, naive and optimal protocols always cross each other at the mechanical barrier's location, $\theta_0 = 60^o$, while in the former case, depending on the details of the energy landscape, the crossing point shifts toward the higher energy state (i.e. towards 120^o).

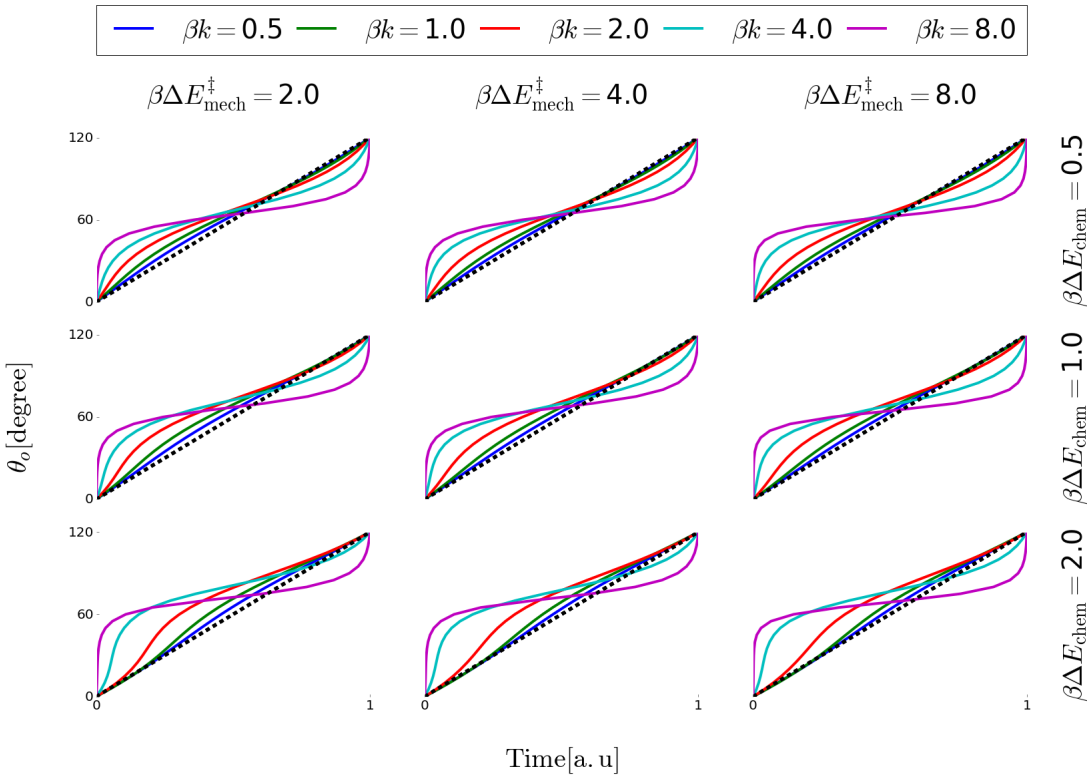

Figure 4.10: Control parameter angle θ_0 as a function of time (in arbitrary units), for naive constant-velocity protocols (black dashed lines) and optimal protocols under the linear-response approximation (solid curves). Chemical energy barrier height $\Delta E^{\ddagger}_{\text{chem}} = 2\ k_{\text{B}}T$. Same variation of k, $\Delta E^{\ddagger}_{\text{mech}}$, and ΔE_{chem} as in Fig. 4.8.

In other words, having $\Delta E_{\text{chem}} \neq 0$ breaks the symmetry of the energy profile around the mechanical energy barriers, leading to a non-symmetric generalized friction coefficient,

optimal driving velocity, and optimal driving protocol around the location of mechanical energy barriers.

4.7.3 Net rotation

In this section, we examine in the tilted energy landscapes the net rotation $\overline{n}$ of the system, in order to understand how a given tilt may affect the system diffusion across the energy landscape. It is also interesting to observe how/when optimal driving protocols and naive driving protocols have different effects on system diffusion.

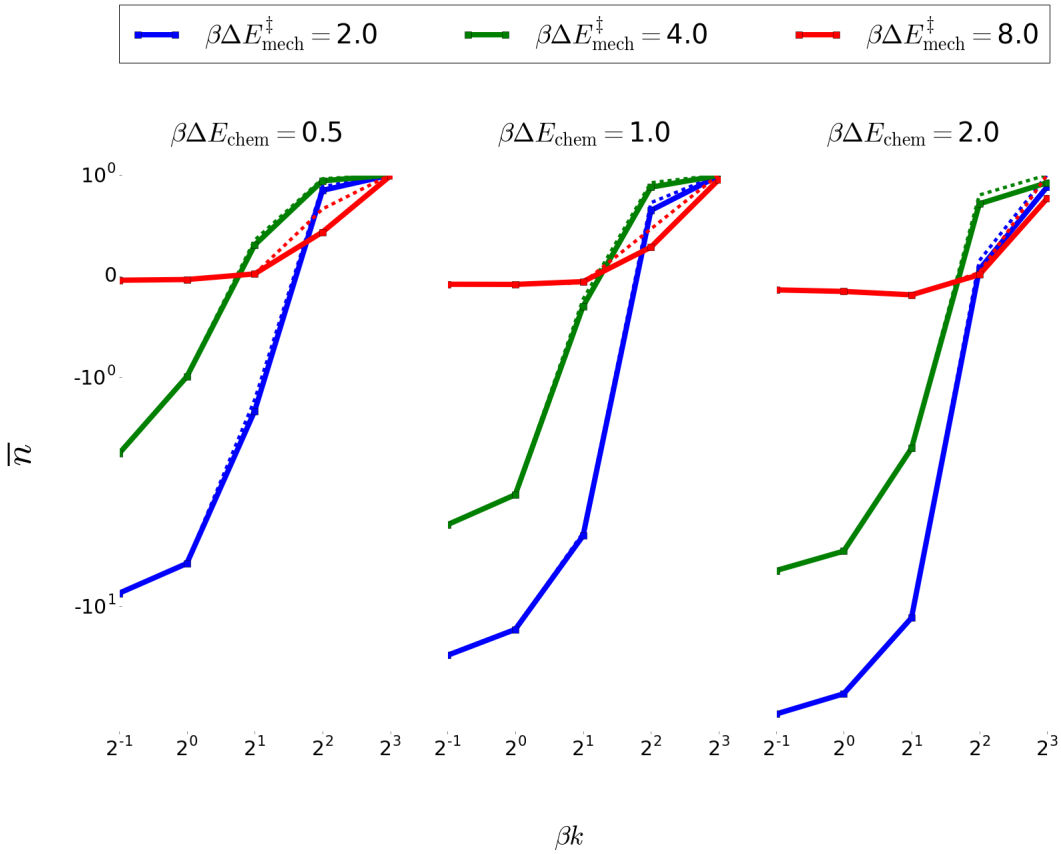

Figure 4.11: System net rotation per one cycle of driving protocol for optimal driving protocols (dashed curves) and naive (constant-velocity) driving protocols (solid curves). Chemical energy barrier height $\Delta E^{\ddagger}_{\mathrm{chem}} = 2\ k_{\mathrm{B}}T$. Same variation of k, $\Delta E^{\ddagger}_{\mathrm{mech}}$, and ΔE_{chem} as in Fig. 4.8.

As shown in Fig. 4.11, there exists a critical trap strength, where on average the spontaneous rotation of the motor due to the tilting force is canceled by the external driving forces, giving $\overline{n} \approx 0$.

For trap strength greater than the critical value, the system starts to operate in the reverse, energetically unfavorable direction, producing high-energy ATP molecules from low-energy ADP molecules. Within the examined range, net rotation varies from roughly

-10^2 rotation to almost exactly $+1$ rotations per one rotation of magnetic trap, where the latter represents the tightly-coupled regime where the system's rotation is completely alongside the trap. Intuitively, the trap drags the system alongside when the perturbation is sufficiently strong to make the forward state more energetically favorable. In addition to the criterion of trap strength, protocol velocity must also provide sufficient time such that the diffusive motion of the system can relax across barriers in reaction to the time-dependent perturbations.

As shown in Fig. 4.10, in the regime of parameters that we have explored, for weak magnetic fields, optimal driving protocols are not significantly different from the naive (constant-velocity) driving protocols, and thus the system's net rotation is not a sensitive function of the driving protocols (Fig. 4.11). However for strong magnetic fields, the system's net rotation during the optimal and naive protocols is distinguishable.

Furthermore, for large mechanical energy barriers ($\sim 8\ k_{\mathrm{B}}T$, red curves in Fig. 4.11, the system basically does not rotate during the protocol, except for really strong perturbation ($k > 4\ k_{\mathrm{B}}T$).

Since the nonequilibrium steady state distribution is characterized by a time-independent current of probability, system net rotation scales up and down as we increase the tilt ΔE_{chem} in the energy landscape. In other words, by increasing the tilt the system would naturally diffuse to the lower energy states and external force can not drag the system towards the higher energy states. This effect of having a tilt is much more clear when weak external perturbation is imposed on the system rather than a strong external driving force because a strong magnetic trap dwarfs the contribution of the tilt.

Chapter 5

Conclusion

In line with the recent growing interest in calculating nonequilibrium properties of stochastic small systems, we have used a recently developed approximate linear-response framework [17, 12] to describe optimal (minimum-dissipation) driving protocols of a stochastic model system that can represent rotary mechanochemical molecular motors, such as F_1 ATP synthase, in which mechanical motion of the motor is tightly coupled to progress in a chemical reaction. According to the mentioned theoretical framework, nonequilibrium excess power as well as optimal driving protocols in the near-equilibrium regime can be evaluated by calculation of a generalized friction tensor (the time integral of the force correlation function).

In our investigation of this rotary mechanochemical molecular motor, the optimal driving velocities (Fig. 4.2) can vary by several orders of magnitude across a given protocol, leading to optimal driving protocols that deviate significantly from naive (constant-velocity) protocols (Fig. 4.3). In particular, a stochastic system generally dissipates less extra energy during a nonequilibrium process if the external driving proceeds rapidly up to the mechanical energy barriers, then slows down around the energy barrier to provide time for thermal fluctuation to effectively kick the system over the mechanical energy barrier.

We have shown that in a simple periodic model system, this linear-response approximation is more accurate when the system is driven out of equilibrium in slower protocols. Although we have only considered a single degree of freedom for the system control parameter, the extension to multiple degrees of freedom could be investigated as well, through multidimensional optimization methods, as has recently been done for a two-dimensional optimal protocol driving an Ising model [14].

F_1 ATP synthase can be experimentally driven in similar ways, where the time-dependent sinusoidal potential is provided through the interaction of a magnetic field and a magnetic bead attached to the central crankshaft of the motor, such that the rotation of the magnetic field drives F_1 alongside the magnetic bead over a sequence of mechanical energy barriers separating metastable states. Therefore, current experimental tools are capable of testing

these general predictions regarding the driving protocols near equilibrium or near nonequilibrium steady-state distributions. Experimentalists can in general hold the magnetic trap constant at different angles θ_0 and measure the ensuing force, and force-force autocorrelation function, to approximately determine the key quantity, the generalized friction coefficient.

Success in the previous experimental tests would strengthen the utility of this new theoretical framework and subsequent approximations and suggestions regarding the modeling of efficient driven stochastic machines. This model system could also help identify parameter regimes which yield the best experimental distinguishability between optimal and naive driving protocols.

In this work, the characterization of optimal protocols requires considerable computational time to calculate the force-force autocorrelation function, making exploration of higher energy barriers more difficult. Therefore, description of optimal driving protocols in more realistic energy landscapes corresponding to the actual F_1 ATP synthase is computationally very hard. To achieve this, we either need to develop different methods for describing optimal driving protocols (such as a recent methods developed for simpler systems [60]), or we can develop special methods for approximation of slow relaxing correlation functions [72].

Furthermore, as demonstrated in Fig. 4.5, optimal protocols remain closer to equilibrium regime than naive driving protocols, and hence are expected to be a set of more appropriate protocol candidates for the investigation of small stochastic systems under near-equilibrium theoretical frameworks [67].

Biological systems including F_1 ATP synthase are naturally driven by thermal fluctuations, rather than single-molecule experiments, so they experience stochastic rather than deterministic driving protocols. In this thesis, we have optimized a mechanochemical system's performance if it can be driven according to a deterministic time schedule. It would be interesting to optimize stochastic protocols as well and observe if any biological systems have been evolutionarily tuned for efficient finite-time operations in the fluctuating cellular environment.

Bibliography

[1] P. Nelson, *Biological Physics: Energy, Information, Life* (W. H. Freeman, 2003).

[2] A. B. Kolomeisky, M. E. Fisher, Annu. Rev. Phys. Chem. **58**, 675-695 (2007).

[3] E. H. Feng, G. E. Crooks. Phys. Rev. Lett., **101**(9), 090602 (2008).

[4] J. Howard, *Mechanics of Motor Proteins and the Cytoskeleton* (Sinauer, Sunderland, MA, 2001).

[5] R. Phillips, J. Kondev, J. Theriot, H. Garcia, Physical Biology of the Cell (Garland Science 2012).

[6] J. R. Moffitt, Y. R. Chemla, S. B. Smith, C. Bustamante, Biochemistry, **77**(1) (2008).

[7] G. Nicolis, I. Prigogine, *Self-Organization in Nonequilibrium Systems* (Wiley, New York, 1997).

[8] M. Yoshida, E. Muneyuki, T. Hisabori, Nat. Rev. Mol. Cell Biol., **2**(9), 669-667 (2001).

[9] R. Yasuda, H. Noji, K. Kinosita, M. Yoshida, Cell, **93**(7), 1117-1124 (1998).

[10] P.R. Zulkowski, D.A. Sivak, M.R. DeWeese, PloS one, **8**(12), p.e82754 (2013).

[11] P.R. Zulkowski, M.R. DeWeese, Phys. Rev. E., **92**(3), (2015).

[12] D. Mandal, C. Jarzynski, J. Stat. Phys., **2016**, (2016).

[13] G.M Rotskoff, G.E. Crooks, and E. Vanden-Eijnden, arXiv: 1607.07425 (2016).

[14] G. M. Rotskoff, G. E. Crooks, Phys. Rev. E., **92**(6), (2015).

[15] M. Schliwa, G. Woehlke, Nature, **422**, 6933 (2003).

[16] P. R. Zulkowski, D. A. Sivak, G. E. Crooks, M. R. DeWeese, Phys. Rev. E., **86**(4), 041148 (2012).

[17] D. A. Sivak, G. E. Crooks, Phys. Rev. Lett., **108**, 190602 (2012).

[18] R. D. Astumian, Science, **276**(5314), 917-922 (1997).

[19] M. Kollmann, L. Lovdok, K. Bartholome, J. Timmer, V. Sourjik, Nature, **438**(7067) (2005).

[20] C. Bustamante, D. Keller, G. Oster, Acc. Chem. Res., **34**(6), 412-420 (2001).

[21] R.D. Astumian, Phys. Chem. Chem. Phys., **9**(37), 5067-5083 (2007).

[22] D. A. Sivak, G. E. Crooks, arXiv: 1608.04444 (2016).

[23] H. Hess, G. D. Bachand, Nanotoday, **8**, 22-29 (2005).

[24] H. Yan, X. P. Zhang, Z. Y. Shen, N. C. Seeman, Nature, **415**, 62-65 (2002).

[25] H. Hess, V. Vogel, Rev. Mol. Biotechnol., **82**, 67-85, (2001).

[26] P. D. Boyer, Annu. Rev. Biochem., **66**, 717-749 (1997).

[27] D. Stock, G. W. Leslie, J. Walker. Science, **286**(5445), 1700-1705 (1999).

[28] R. Yasuda, H. Noji, M. Yoshida, K. Kinosita, H. Itoh, Nature, **410**(6831), 898-904 (2001).

[29] D. Spetzler, J. York, D. Daniel, R. Fromme, D. Lowry, W. Frasch, Biochemistry, **45**(10), 3117-3124 (2006).

[30] R. Ishmukhametov, T. Hornung, W. D. Frasch, EMBO J., **29**(23), 3911-3923 (2010).

[31] D. Spetzler, R. Ishmukhametov, T. Hornung, L. J. Day, J. Martin, W. D. Frasch. Bio. Chem., **48**(33), 7979-7985 (2009).

[32] Y. Hirono-Hara, H. Noji, M. Nishiura, E. Muneyuki, K. Y. Hara, R. Yasuda, J. K. Kinosita, M. Yoshida, Proc. Natl. Acad. Sci. USA, 98, 649-654 (2001).

[33] H. Itoh, A. Takahashi, K. Adachi, H. Noji, R. Yasuda, M. Yoshida, K. Kinosita, Nature, **427**, 465-468 (2004).

[34] Y. Rondelez, G. Tresset, T. Nakashima, Y. Kato-Yamada, H. Fujita, S. Takeuchi, H. Noji, Nature, **433**, 773-777 (2005).

[35] A. Wachter, Y. Bi, S. D. Dunn, B. D. Cain, H. Sielaff, F. Wintermann, S. Engelbrecht, W. Junge, Proc. Natl. Acad. Sci. USA, 108, 3924- 3929 (2011).

[36] H. Sielaff, H. Rennekamp, A. Wachter, H. Xie, F. Hilbers, K. Feldbauer, S. D. Dunn, S. Engelbrecht, W. Junge, Proc. Natl. Acad. Sci. USA, 105, 760-765 (2009).

[37] K. I . Okazaki, G. Hummer, Proc. Natl. Acad. Sci. USA, **112**(34), 10720-10725 (2015).

[38] K. Svoboda, C. F. Schmidt, B. J. Schnapp, S. M. Block, Nature, **365**(6448), 721 - 727 (1993).

[39] H. Wang, G. Oster, Nature, 396(6708), 279-282 (1998).

[40] T. M. Cover, J. A. Thomas. Elements of Information Theory, Wiley, New York, 2006.

[41] B. Gaveau, L. A. Schulman, Phys. Lett. A, **229**, 347-353 (1997).

[42] D. A. Sivak, G. E. Crooks, Phys. Rev. Lett., **108**, 150601 (2012).

[43] G. E. Crooks, Fisher Information and Statistical Mechanics. Tech. Rep, 2011.

[44] P.R. Zulkowski, D.A. Sivak, G.E. Crooks, and M.R. DeWeese, Physical Review E, **86**(4) (2012).

[45] D. Stock, C. Gibbons, I. Arechaga, A. G. Leslie, J. E. Walker, Curr. Opin. Struct. Biol., **10**(6), 672-679 (2000).

[46] W. Junge, H. Lill, S. Engelbrecht, Trends. Biochem. Sci., **22**(11), 420-423 (1997).

[47] M. Wikstrom, Curr. Opin. Struct. Biol., **8**(4), (1998).

[48] T. C. Elston, G. Oster, Biophys. J., **73**(2), 703, (1997).

[49] D. L. Foster, R. H. Fillingame, J. Biol. Chem., **257**(4), 1982.

[50] J. W. Gibbs, *Elementary Principles in Statistical Mechanics* (Courier Corporation, 2014).

[51] D. Chandler, *Introduction to Modern Statistical Mechanics* (Oxford University Press, 1987).

[52] R. Zwanzig, *Nonequilibrium Statistical Mechanics* (Oxford University Press, 2001).

[53] P. Hanggi, P. Talkner, and M. Borkovec, Rev. Mod. Phys., **62**(2), 251 (1900).

[54] C. Jarzynski, Phys. Rev. Lett., **78** 2690 (1997).

[55] C. Jarzynski, Phys. Rev. E., **56** 5018 (1997).

[56] G. E. Crooks, Phys. Rev. E., **60**, 2721 (1999).

[57] G. E. Crooks, Phys. Rev. E., **61** 2361 (2000).

[58] C. Jarzynski, arXiv: 9802155 (1998).

[59] C. Jarzynski, Comptes Rendus Physique, **8**(5), 495-506 (2007).

[60] P. R. Zulkowski, M. R. DeWeese, Phys. Rev. E., **92**, 032117 (2015).

[61] A. Berezhkovskii and A. Szabo, J. Chem. Phys., **135**, 074108 (2011).

[62] T. Schmiedl, U. Seifert. Phys. Rev. Lett., **98**(10), 108301 (2007).

[63] A. Gomez-Marin, T. Schmiedl, U. Seifert. J. Chem. Phys., **129**(2), 024114 (2008).

[64] P. R. Zulkowski, M. R. DeWeese, Phys. Rev. E, **92**(3), 032117 (2015).

[65] G. B. Arfken, H. J. Weber, F. E. Harris, *Mathematical Methods for Physicists: A Comprehensive Guide* (Academic Press, 2011).

[66] N. J. Carter, R. A. Cross, Nature, **435**, 308 (2005).

[67] J. Gore, F. Ritort, C. Bustamante. Proc. Natl. Acad. Sci. USA, 100, 12564 (2003).

[68] H. C. Berg, *Random Walks in Biology* (Princeton University Press, 1993).

[69] Y. Oono, M. Paniconi, Prog. Theor. Phys. Suppl., **130**, 29-44 (1998).

[70] M. Esposito, C. V. Broeck, Eur. Phys. Lett. **95**, 40004 (2011).

[71] S. Still, D. A. Sivak, A. J. Bell, and G. E. Crooks, Phys. Rev. Lett., **109**, 120604 (2012).

[72] M. V. S. Bonanca, S. Deffner, J. Chem. Phys., 140, 244119 (2014).

Appendix A

Ratio of optimal and naive excess works

Here we summarize a derivation originally presented in [22]. In sufficiently slow driving protocols where linear-response theory is applicable, the excess work, during a nonequilibrium driving protocol, is the time integral of the generalized friction coefficient times the square of the control parameter velocity [17]. By calculating friction coefficients across the control parameter space in a discrete set of N equally spaced points and considering a piecewise constant-velocity protocol in each time-step, this integral can be approximated by a discrete sum:

$$W_{\mathrm{ex}} = \int \mathrm{d}t \left(\frac{\mathrm{d}\lambda}{\mathrm{d}t}\right)^2 \zeta[\lambda(t)] \tag{A.1a}$$

$$\approx \sum_j \Delta t_j \left(\frac{\mathrm{d}\lambda}{\mathrm{d}t}\bigg|_{t_j}\right)^2 \zeta[\lambda(t_j)] \tag{A.1b}$$

$$= \sum_j \frac{\frac{\Delta\lambda}{N}}{\frac{\mathrm{d}\lambda}{\mathrm{d}t}\Big|_{t_j}} \left(\frac{\mathrm{d}\lambda}{\mathrm{d}t}\bigg|_{t_j}\right)^2 \zeta_j \tag{A.1c}$$

$$= \frac{\Delta\lambda}{N} \sum_j \frac{\mathrm{d}\lambda}{\mathrm{d}t}\bigg|_{t_j} \zeta_j \ . \tag{A.1d}$$

For the naive (constant-velocity) protocol, the excess work is proportional to the average friction coefficient:

$$W_{\mathrm{ex}}^{\mathrm{naive}} = \frac{(\Delta\lambda)^2}{N\Delta t} \sum_j \zeta_j = \frac{(\Delta\lambda)^2}{\Delta t} \ \overline{\zeta} \ . \tag{A.2}$$

The optimal protocol velocity is proportional to the inverse square root of the friction coefficient, and the proportionality constant can be found by constraining the protocol to

finish in the allotted time interval Δt:

$$\Delta t = \sum_j \frac{\frac{\Delta\lambda}{N}}{\left.\frac{\mathrm{d}\lambda^{\mathrm{opt}}}{\mathrm{d}t}\right|_{t_j}} \tag{A.3a}$$

$$= \sum_j \frac{\frac{\Delta\lambda}{N}}{A\ \zeta_j^{-1/2}} \tag{A.3b}$$

$$= \frac{\Delta\lambda}{A} \frac{\sum_j \zeta_j^{1/2}}{N} \tag{A.3c}$$

$$= \frac{\Delta\lambda}{A}\ \overline{\zeta^{1/2}}\ . \tag{A.3d}$$

Therefore, the proportionality constant is

$$A = \frac{\Delta\lambda}{\Delta t}\ \overline{\zeta^{1/2}}\ , \tag{A.4}$$

and the excess work on the optimal protocol is

$$W_{\mathrm{ex}}^{\mathrm{opt}} = \frac{\Delta\lambda}{N} \sum_j (A\zeta_j^{-1/2})\zeta_j \tag{A.5a}$$

$$= \frac{(\Delta\lambda)^2}{N\Delta t} \overline{\zeta^{1/2}} \sum_j \zeta_j^{1/2} \tag{A.5b}$$

$$= \frac{(\Delta\lambda)^2}{\Delta t} \overline{\zeta^{1/2}}^2\ . \tag{A.5c}$$

In conclusion, the ratio of naive and optimal excess works is

$$\frac{W_{\mathrm{ex}}^{\mathrm{naive}}}{W_{\mathrm{ex}}^{\mathrm{opt}}} = \frac{\overline{\zeta}}{\overline{\zeta^{1/2}}^2}\ . \tag{A.6}$$